THE HALO OCCUPATION DISTRIBUTION AND THE PHYSICS OF GALAXY FORMATION

Andreas A. Berlind,[1] David H. Weinberg,[2] Andrew J. Benson,[3] Carlton M. Baugh,[4] Shaun Cole,[4]
Romeel Davé,[5] Carlos S. Frenk,[4] Adrian Jenkins,[4] Neal Katz,[6] and Cedric G. Lacey[4,7]

ABSTRACT

The halo occupation distribution (HOD) describes the bias between galaxies and dark matter by specifying (1) the probability $P(N|M)$ that a halo of virial mass M contains N galaxies of a particular class and (2) the relative spatial and velocity distributions of galaxies and dark matter within halos. We calculate and compare the HODs predicted by a smoothed particle hydrodynamics (SPH) simulation of a ΛCDM cosmological model (cold dark matter with a cosmological constant) and by a semianalytic galaxy formation model applied to the same cosmology. Although the two methods predict different galaxy mass functions, their HOD predictions for samples of the same space density agree remarkably well. In a sample defined by a baryonic mass threshold, the mean occupation function $\langle N \rangle_M$ exhibits a sharp cutoff at low halo masses, a slowly rising plateau in which $\langle N \rangle$ climbs from 1 to 2 over nearly a decade in halo mass, and a more steeply rising high-occupancy regime at high halo mass. In the low-occupancy regime, the factorial moments $\langle N(N-1) \rangle$ and $\langle N(N-1)(N-2) \rangle$ are well below the values of $\langle N \rangle^2$ and $\langle N \rangle^3$ expected for Poisson statistics, with important consequences for the small-scale behavior of the two- and three-point correlation functions. The HOD depends strongly on galaxy age, with high-mass halos populated mainly by old galaxies and low-mass halos by young galaxies. The distribution of galaxies within SPH halos supports the assumptions usually made in semianalytic calculations: the most massive galaxy lies close to the halo center and moves near the halo's mean velocity, while the remaining, satellite galaxies have the same radial profile and velocity dispersion as the dark matter. The mean occupation at fixed halo mass in the SPH simulation is independent of the halo's larger scale environment, supporting both the merger tree approach of the semianalytic method and the claim that the HOD provides a complete statistical characterization of galaxy bias. We discuss the connections between the predicted HODs and the galaxy formation physics incorporated in the SPH and semianalytic approaches. These predictions offer useful guidance to theoretical models of galaxy clustering, and they will be tested empirically by ongoing analyses of galaxy redshift surveys. By applying the HODs to a large-volume N-body simulation, we show that both methods predict slight departures from a power-law galaxy correlation function, similar to features detected in recent observational analyses.

Subject headings: cosmology: theory — galaxies: formation — galaxies: halos —
large-scale structure of universe

1. INTRODUCTION

A complete theory of galaxy formation should predict the distributions of galaxy luminosities, colors, sizes, and morphologies, the correlations among these properties, and the relation between the spatial clustering of any given class of galaxies and that of the underlying dark matter distribution. This last class of predictions, the "bias" of galaxies as a function of their observable properties, is becoming an increasingly important test of theoretical models thanks to the new generation of large galaxy redshift surveys, in particular the Two-Degree Field Galaxy Redshift Survey (2dFGRS; Colless et al. 2001) and the Sloan Digital Sky Survey (SDSS; York et al. 2000). The halo occupation distribution (HOD) formalism is an especially powerful framework for carrying out such tests; it characterizes the bias of a class of galaxies by the probability $P(N|M)$ that a halo of virial mass M contains N such galaxies and additional prescriptions that specify the relative distributions of galaxies and dark matter within halos. If the HOD at fixed halo mass is statistically independent of the halo's large-scale environment, as theoretical models predict (Bond et al. 1991; White 1996; Lemson & Kauffmann 1999; this paper), then this description of galaxy bias is essentially complete: given the HOD and the halo population predicted by a particular cosmological model, one can calculate any galaxy-clustering statistic, on scales from the linear regime to the deeply nonlinear regime. Empirical determinations of the HOD for different galaxy types would therefore summarize in a form that can be readily compared with theoretical predictions everything that observed galaxy clustering has to say about the physics of galaxy formation.

This paper examines the HODs predicted by the two leading theoretical methods for studying galaxy formation and

[1] Center for Cosmological Physics and Department of Astronomy and Astrophysics, 5640 South Ellis Avenue, University of Chicago, Chicago, IL 60637; aberlind@oddjob.uchicago.edu.

[2] Department of Astronomy, Ohio State University, 140 West 18th Avenue, Columbus, OH 43210; dhw@astronomy.ohio-state.edu.

[3] Department of Astronomy, MS 105-24, California Institute of Technology, 1201 East California Boulevard, Pasadena, CA 91125; abenson@astro.caltech.edu.

[4] Institute for Computational Cosmology, University of Durham, Durham DH1 3LE, UK; c.m.baugh@durham.ac.uk, shaun.cole@durham.ac.uk, c.s.frenk@durham.ac.uk, a.r.jenkins@durham.ac.uk.

[5] Steward Observatory, 933 North Cherry Avenue, University of Arizona, Tucson, AZ 85721; rad@as.arizona.edu.

[6] Department of Physics and Astronomy, University of Massachusetts, 710 North Pleasant Street, Amherst, MA 01003; nsk@kaka.phast.umass.edu.

[7] Observatoire de Lyon, 9 Avenue Charles Andre, 69230 Saint Genis Laval, France; lacey@obs.univ-lyon1.fr.

bias in a cosmological context: semianalytic models (e.g., White & Frenk 1991; Kauffmann, White, & Guideroni 1993; Cole et al. 1994; Avila-Reese, Firmani, & Hernandez 1998; Somerville & Primack 1999) and hydrodynamic numerical simulations (e.g., Cen & Ostriker 1992; Katz, Hernquist, & Weinberg 1992; Evrard, Summers, & Davis 1994; Pearce et al. 1999; White, Hernquist, & Springel 2001; Yoshikawa et al. 2001). We apply both methods to a ΛCDM mological model (inflationary cold dark matter with a cosmological constant), adopting the same cosmological parameters in each case. We focus on galaxy samples defined by thresholds in baryon mass and stellar population age, which are roughly analogous to observational samples defined by cuts in luminosity and color. Except for using the same cosmological model and thus the same present-day halo population, we do not make any efforts to "tune" the semianalytic calculation to match the hydrodynamic simulation; we apply each method in its "standard" form. We present results for the various features of the HOD—the mean occupation $\langle N \rangle$ as a function of halo mass, moments of the distribution $P(N|\langle N \rangle)$, and the spatial and velocity distributions of galaxies within halos—and we interpret these features in terms of the physical processes represented in the theoretical models. In the short term, our results should provide useful input to theoretical models of galaxy clustering by allowing the predictions of these galaxy formation models to be "bootstrapped" into analytic calculations or larger volume N-body simulations, and they offer guidance to efforts to infer parameters of the HOD from observational data. In the slightly longer term, these predictions will be tested by empirical determinations of the HOD, and any discrepancies with observations may point the way to necessary revisions of the galaxy formation model or the underlying cosmological model.

Several aspects of the HOD predicted by semianalytic models have been investigated in the pioneering papers of Kauffmann, Nusser, & Steinmetz (1997), Governato et al. (1998), Kauffmann et al. (1999), and Benson et al. (2000b), which used semianalytic methods to assign galaxy populations to the halos of N-body simulations. Seljak (2000) and Sheth & Diaferio (2001) measured $P(N|M)$ from the Kauffmann et al. (1999) models and incorporated them into analytic predictions of galaxy clustering and bias (see also Scoccimarro et al. 2001; Sheth et al. 2001a; Scranton 2002). HOD predictions of hydrodynamic simulations have been presented by White et al. (2001) at redshifts $z = 3$ and $z = 1$ and by Yoshikawa et al. (2001) at $z = 3$, 2, and 0. Relative to this earlier work, our examination of the HOD in this paper is more comprehensive, and our side-by-side comparison of numerical and semianalytic results for the same cosmological model allows us to evaluate the robustness and limitations of the predictions and to better understand the physics that gives rise to them.

Other studies of the halo occupation distribution have focused on the connections between the HOD and statistical measures of galaxy clustering. Many of these studies have utilized the power of the HOD formalism and the related "halo model" of dark matter clustering as a tool for analytic calculations (Ma & Fry 2000; Seljak 2000; Benson 2001; Scoccimarro et al. 2001; Sheth et al. 2001a; White 2001; Cooray & Sheth 2002), drawing on methods developed over the course of several decades (Neyman & Scott 1952; Peebles 1974; McClelland & Silk 1977; Scherrer & Bertschinger 1991; Mo & White 1996; Sheth, Mo, &

Tormen 2001b). Berlind & Weinberg (2002, hereafter BW) computed the impact of HOD bias on many of the most widely used galaxy-clustering statistics by applying parameterized HOD models to an N-body simulation of the ΛCDM scenario. They concluded that different statistics constrain the HOD in complementary ways, making it possible to determine the HOD empirically from observed galaxy clustering, at least for a known cosmological model. Important steps toward observational determination of the HOD of bright optically selected galaxies, drawing mainly on the two- and three-point correlation functions, the group multiplicity function, and galaxy-galaxy lensing, have been taken by Jing, Mo, & Börner (1998), Peacock & Smith (2000), Scoccimarro et al. (2001), Guzik & Seljak (2002), Marinoni & Hudson (2002), Yang, Mo, & van den Bosch (2003), van den Bosch, Yang, & Mo (2003), Zehavi et al. (2003), and Magliocchetti & Porciani (2003). Kochanek et al. (2003), Jing, Börner, & Suto (2002), and Cooray (2002) have investigated HOD constraints for galaxies selected in the near- or far-infrared, and Wechsler et al. (2001), Bullock, Wechsler, & Somerville (2002), and Moustakas & Somerville (2002) have applied similar methods to high-redshift galaxies. An ambitious but, we think, realizable goal is to use the high-precision measurements afforded by the 2dFGRS and the SDSS to break the "degeneracies" between cosmology and bias, obtaining tight, simultaneous constraints on the mass function and clustering of dark halos and the HODs of many different galaxy classes (see discussions by BW, Zheng et al. 2002, and Weinberg 2002). We hope that the results presented here will provide inspiration to such efforts, by illustrating how measurements of the HOD can test basic ideas about the physics of galaxy formation.

Our approach to the HOD is essentially the one described by BW, which was in turn inspired largely by the discussion of Benson et al. (2000a, 2000b). The clustering of galaxies predicted by the semianalytic model and hydrodynamic simulation investigated here, as quantified by more traditional statistics, has been presented in separate papers (Benson et al. 2000b; Weinberg et al. 2002). We briefly describe the two calculations and the selection of galaxy populations in § 2. In § 3 we compare the predictions of $P(N|M)$ for several different galaxy classes, and we demonstrate that $P(N|M)$ predicted by the hydrodynamic simulation is independent of the large-scale environment, to within the statistical limitations of our measurements. Semianalytic models do not predict the distribution of galaxies within halos, but clustering calculations on the basis of these models usually assume that each halo contains one central galaxy moving at the halo's center-of-mass velocity and that other "satellite" galaxies trace the halo's dark matter distribution. In § 4, we show that these assumptions hold to a good approximation in the hydrodynamic simulation, which predicts the galaxy positions and velocities directly. In § 5 we compare the properties of central and satellite galaxies in the two methods. The precision in predictions of the galaxy correlation function by these two models has been limited by the finite size of the simulation volumes in which they were implemented. In § 6 we combine the HOD results with a new, large-volume N-body simulation to make improved predictions for the galaxy correlation function, focusing on predicted departures from a power-law form. In § 7 we summarize our results and discuss what they tell us about the physical factors that shape the HOD and thereby determine the bias between galaxies and dark matter.

2. THEORETICAL MODELS

2.1. *SPH Simulation*

We use a smoothed particle hydrodynamics (SPH) simulation of a ΛCDM cosmological model, with $\Omega_m = 0.4$, $\Omega_\Lambda = 0.6$, $\Omega_b = 0.02 \, h^{-2}$, $h \equiv H_0/(100 \text{ km s}^{-1} \text{ Mpc}^{-1}) = 0.65$, $n = 0.95$, and $\sigma_8 = 0.8$. This model is in good agreement with a wide variety of cosmological observations (see, e.g., Spergel et al. 2003), though the value of Ω_m is somewhat higher than that favored by the most recent constraints. In terms of HOD predictions, lowering Ω_m while keeping other parameters fixed would primarily shift the mass scale of halos by a constant factor (Zheng et al. 2002), though the change of dynamical growth timescales relative to gas cooling timescales could have a secondary influence. The simulation uses the Parallel TreeSPH code (Hernquist & Katz 1989; Katz, Weinberg, & Hernquist 1996; Davé, Dubinski, & Hernquist 1997) to follow the evolution of 144^3 gas and 144^3 dark matter particles in a $50 \, h^{-1}$ Mpc box from $z = 49$ to $z = 0$. The mass of each dark matter particle is $6.3 \times 10^9 \, M_\odot$, the mass of each baryonic particle is $8.5 \times 10^8 \, M_\odot$, and the gravitational force softening is $\epsilon_{\text{grav}} = 7 \, h^{-1}$ kpc (Plummer equivalent). As a test of numerical resolution effects, in § 3 we also show results from a simulation of a $22.222 \, h^{-1}$ Mpc cube with a factor of 8 higher mass resolution (2×128^3 particles) and a gravitational softening of $3.5 \, h^{-1}$ kpc.

Dark matter particles are affected only by gravity, whereas gas particles are subject to pressure gradients and shocks, in addition to gravitational forces. The TreeSPH code includes the effects of both radiative and Compton cooling. TreeSPH also includes heating by a background UV radiation field but we include only its effects in the simulation of the $22.222 \, h^{-1}$ Mpc cube. We cannot accurately include a background UV radiation field at the lower resolution of the $50 \, h^{-1}$ Mpc simulation (Weinberg, Hernquist, & Katz 1997). Star formation is assumed to happen in regions that are Jeans-unstable and where the gas density is greater than a threshold value ($n_H \geq 0.1 \text{ cm}^{-3}$) and colder than a threshold temperature ($T \leq 30,000$ K). Once gas is eligible to form stars, it does so at a rate proportional to $\rho_{\text{gas}}/t_{\text{gas}}$, where ρ_{gas} is the gas density and t_{gas} is the longer of the gas cooling and dynamical times. Gas that turns into stars becomes collisionless and releases energy back into the surrounding gas via supernova explosions. A Miller-Scalo (1979) initial mass function of stars is assumed, and stars of mass greater than $8 \, M_\odot$ become supernovae and inject 10^{51} ergs of pure thermal energy into neighboring gas particles. The star formation and feedback algorithms are discussed extensively by Katz et al. (1996), and the particular simulations employed here are described in greater detail by Murali et al. (2002), Davé, Katz, & Weinberg (2002), and Weinberg et al. (2002). The parameters are all chosen on the basis of a priori theoretical and numerical considerations and are not adjusted to match any observations.

SPH galaxies are identified at the sites of local baryonic density maxima by using the SKID algorithm,[8] which selects gravitationally bound groups of star and cold dense gas particles. Because dissipation greatly increases the density contrast of these baryonic components, there is essen-

tially no ambiguity in the identification of galaxies. We retain only those particle groups whose mass exceeds a threshold $M_{b,\text{min}} = 5.42 \times 10^{10} \, M_\odot$, corresponding to the mass of 64 SPH particles, and the resulting galaxy space density is $\bar{n}_g = 0.02 \, h^3 \text{ Mpc}^{-3}$. We also construct lower density (and thus more massive) samples with $\bar{n}_g = 0.01 \, h^3$ Mpc^{-3} and $\bar{n}_g = 0.005 \, h^3 \text{ Mpc}^{-3}$, which have minimum baryonic masses of 1.25×10^{11} and $2.39 \times 10^{11} \, M_\odot$, respectively. The galaxy properties that we use in this analysis, aside from position and velocity, are the total baryonic mass and the median stellar age (i.e., the look-back time to the point at which half the stellar mass had formed).

We identify dark matter halos in the mass distribution by using a friends-of-friends algorithm (Davis et al. 1985) with a linking length of 0.173 times the mean interparticle separation, and we consider only halos consisting of at least 32 dark matter particles. We choose this particular linking length because, for this cosmological model, it most closely corresponds to the definition of a halo assumed in the semianalytic model described in the following section. We assume a universal baryon-to-matter ratio and scale halo dark matter masses up by a factor of $\Omega_m/(\Omega_m - \Omega_b) = 1.134$ to obtain total halo masses. The minimum halo mass we resolve is therefore $2.29 \times 10^{11} \, M_\odot$, and the most massive halo in our $50 \, h^{-1}$ Mpc box is $3.29 \times 10^{14} \, M_\odot$. Finally, we decide halo membership of galaxies by assigning each galaxy to the halo that contains the dark matter particle closest to the galaxy center of mass.

2.2. *Semianalytic Model*

Semianalytic galaxy formation models have their roots in the work of White & Rees (1978), Fall & Efstathiou (1980), Cole (1991), Lacey & Silk (1991), and White & Frenk (1991), who established the basic framework of this approach. The semianalytic (SA) model that we use in this paper is GALFORM, which is described in detail by Cole et al. (2000). The model begins with a population of halo masses that is usually either generated using the Press & Schechter (1974) halo mass function or drawn from an N-body simulation. In this study, we supply the SA model with the same halo population identified in the SPH simulation. The predictions of the two methods can thus be compared halo by halo without being subject to differences caused by sample variance. In addition, we produce 10 SA realizations for each SPH halo so that we can determine the SA $P(N|M)$ relation more accurately.

For each halo, the SA model first employs a Monte Carlo method to generate a "merger tree," which describes the hierarchical growth of that particular halo. The tree starts at $z = 0$ and works backward in time, branching into progenitor halos, until it reaches a starting redshift. The halo merger rates used by the merger tree algorithm are those derived by Lacey & Cole (1993). The merger statistics that underpin the SA model are of particular importance to $P(N|M)$, since the number of galaxies in any given halo should be closely related to the formation and merger history of its progenitor halos. Once a merger tree is created, a suite of analytic prescriptions is used to model the formation and evolution of galaxies in each progenitor halo, starting with the highest-redshift progenitors and moving forward in time all the way to the single halo at $z = 0$.

Each halo is given an NFW (Navarro, Frenk, & White 1996) dark matter density profile (with no scatter in halo

---

[8] See http://www-hpcc.astro.washington.edu/tools/skid.html and Katz et al. 1996.

concentration) and an angular momentum drawn from a lognormal distribution. Diffuse gas is assumed to be shock heated to the halo virial temperature during the formation process and to settle initially into a spherical distribution. Gas that is dense enough to radiate its thermal energy before the halo experiences a major merger is assumed to accrete onto a centrifugally supported disk at the halo center. This mechanism proceeds from the center of the halo outward, since the cooling timescale is an increasing function of radius within the halo. Cold gas that has settled onto the disk begins forming stars at a rate proportional to the total mass of cold disk gas and inversely proportional to an empirical timescale, which is described below. The effects of stellar winds are modeled by returning a fraction of stellar mass into the cold gas phase, and the effects of feedback are parameterized by reheating a fraction of the cold gas to the halo virial temperature and ejecting it from the disk. The SA model keeps track of how much gas is in the hot, cold, and stellar phases at any given time and traces chemical enrichment of the gas by following the exchange of metals among these three phases.

If at any point during this process the merger tree contains a merger between two halos, the most massive galaxy is assumed to become the "central" galaxy of the merged halo and any other galaxies present become "satellites." Each of these satellite galaxies is assigned a random orbit and a timescale on which dynamical friction causes it to merge with the central galaxy. If such a galaxy merger happens, the central galaxy's evolution may be mildly or severely disrupted, depending on the mass ratio M_{sat}/M_{cen} of the merging galaxies. If $M_{sat}/M_{cen} \geq 0.5$, then the merger is classified as "major," and the two galaxies form an elliptical galaxy, with their remaining gas consumed in a single burst of star formation. If $0.5 > M_{sat}/M_{cen} \geq 0.25$, then the star formation burst still happens, but the central galaxy disk is not destroyed. Finally, if $M_{sat}/M_{cen} < 0.25$, then the satellite's gas and stars are added to that of the central galaxy without disrupting it. There are several adjustable parameters in the SA model, and their values are chosen so that the model reproduces some observed properties of the local galaxy population, in particular the galaxy luminosity function. Other observables then serve to test the model. The SA parameters are *not* adjusted on the basis of galaxy-clustering measurements. Yoshida et al. (2002) and Helly et al. (2003) compare the galaxy properties predicted by SA calculations and SPH simulations, and in these tests they adjust the SA parameters to mimic the physical assumptions and numerical resolution of the simulations. Here we have chosen to take both methods "as is"; the SA model incorporates its standard set of physical processes, and its parameters are adjusted on the basis of observations.

The SA model computes many observable properties of galaxies, such as luminosities, sizes, colors, metallicities, and morphological types. The properties that interest us here, in addition to halo membership, are the total baryonic mass and the mass-weighted mean stellar age. We will also make use of the SA bulge-to-disk ratios in § 3.3. While the nature of the semianalytic model used in this work is identical to that described by Cole et al. (2000), the parameters differ from those of their fiducial model because we have adopted different cosmological parameters. In particular, we adopt the baryon density parameter $\Omega_b = 0.02\, h^{-2} = 0.0473$ used in the SPH simulation, where Cole et al. (2000) used $\Omega_b = 0.02$, and we are forced to alter other model parameters to maintain a good match to local galaxy luminosity functions. The star formation timescale in the semianalytic model is now described by

$$\tau_* = \tau_*^0 (V_d/200 \text{ km s}^{-1})^{\alpha_*}, \qquad (1)$$

with $\tau_*^0 = 3$ Gyr and $\alpha_* = -2.5$, and the feedback parameter V_{hot} is increased to 250 km s^{-1}. We also impose a minimum star formation timescale of 1 or 25 Myr for quiescent and bursting star formation, respectively. We adopt the Salpeter initial mass function (IMF) and a recycled fraction $R = 0.373$ (our choice of IMF is not particularly important for this work since we consider only the total stellar mass of galaxies, rather than their photometric properties). The core radius of the gas density profile in the model halos is initially set to $\frac{2}{3}$ of the NFW scale radius (twice as large as in Cole et al. 2000). We inhibit cooling of gas in dark matter halos with virial velocities below 60 km s^{-1} to mimic the effects of an ionizing background. Finally, the critical mass ratios of merging galaxies that determine when elliptical galaxies and bursts of star formation are produced have changed to the values described above (from $M_{sat}/M_{cen} > 0.3$ in Cole et al. 2000). The dependence of SA model predictions on input parameters and modeling assumptions has been examined extensively in other papers (e.g., Kauffmann et al. 1993; Cole et al. 1994, 2000; Somerville & Primack 1999; Benson et al. 2002). We will not attempt such an investigation here, but we note that the good agreement we find between the HOD predictions of the SA model and the SPH simulations, two radically different methods of calculation, suggests that the SA predictions themselves will not be sensitive to the modeling details, at least for models that are tuned to reproduce the observed galaxy luminosity function.

As in the SPH case, we construct three galaxy samples of different space densities by including only galaxies above a baryonic mass threshold. In the SA model these thresholds are $M_{b,min} = 1.45 \times 10^{10}$, 3.14×10^{10}, and $5.67 \times 10^{10}\ M_\odot$ for galaxy samples with space densities of $\bar{n}_g = 0.02$, $\bar{n}_g = 0.01$, and $\bar{n}_g = 0.005\ h^3$ Mpc^{-3}, respectively. These mass thresholds are approximately a factor of 4 lower than the corresponding SPH thresholds, a difference we discuss in the following section.

2.3. Galaxy Mass and Correlation Functions

Figure 1 shows cumulative baryonic mass functions for SPH and SA galaxies, starting at the thresholds that define our main analysis samples, with space density $\bar{n}_g = 0.02\ h^3$ Mpc^{-3}. At any given space density, the SA galaxies are less massive by a factor of 4–10. The parameters of the SA model, primarily those controlling the gas core radius and stellar feedback, are chosen to produce a good fit to the observed galaxy luminosity function. As we will show later, the baryonic mass of the SA galaxies hosted by a given dark matter halo rarely exceeds 25% of the total mass of baryons within the halo virial radius. In the SPH simulations, on the other hand, low-mass halos frequently host a galaxy with $M_b \sim (\Omega_b/\Omega_m)M_h$, corresponding to 100% of the baryon mass within the virial radius. For observationally motivated choices of the stellar mass-to-light ratio, the resulting Tully-Fisher (1977) relation is in reasonable accord with observations, but the predicted luminosity function is too high (N. Katz et al. 2003b, in preparation).

The growing gap between the SA and SPH mass functions in Figure 1 is partly a consequence of numerical
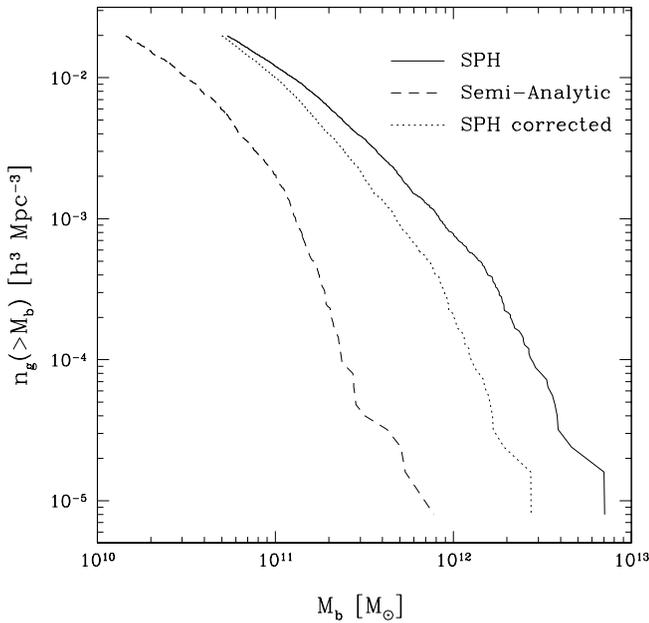
Fig. 1.—Cumulative baryonic mass functions of SPH (*solid curve*) and SA galaxies (*dashed curve*). The dotted curve incorporates a correction for finite resolution effects on the SPH galaxy mass function, estimated by comparing two simulations of a 22.222 h^{-1} Mpc cube.
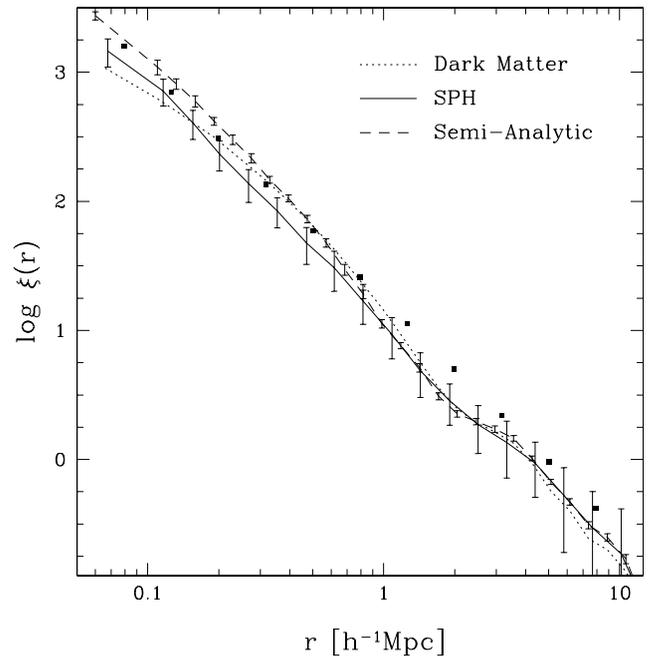

Fig. 2.—Plot of two-point correlation functions of dark matter and model galaxies. The curves show the correlation function of the dark matter in the SPH simulation (*dotted curve*), the SPH galaxies (*solid curve*), and the SA galaxies (*dashed curve*). The points show the fitted power-law relation for 2dF L_* galaxies from Norberg et al. (2002a): $\xi(r) = (r/4.9)^{-1.79}$. The SPH and SA galaxy samples have a space density of $\bar{n}_g = 0.02\ h^3$ Mpc^{-3} and thus correspond to a population of galaxies less luminous than L_*. The error bars shown for the SPH correlation function are the errors in the mean estimated from jackknife resampling using the eight octants of the cube, and they thus include an estimate of "cosmic variance" of the finite number of coherent structures in the simulation volume. The SA correlation function shown is the average over 10 realizations of the SA model, and the error bars are the uncertainty in the mean. The SA error bars thus represent the uncertainty in $P(N|M)$ predicted by the model but do not include cosmic variance.

resolution effects in the SPH simulation. A galaxy-by-galaxy comparison of two simulations in a 22.222 h^{-1} Mpc cube, the 2×128^3 particle simulation mentioned in § 2.1, and a 2×64^3 simulation that has the same resolution as our 2×144^3, 50 h^{-1} Mpc run, indicates that the lower resolution calculations, which also do not include the effects of a photoionizing UV background, yield approximately correct masses for galaxies near the $64m_{\mathrm{SPH}}$ threshold but systematically overestimate the masses of larger galaxies, probably because of the two-phase interface effects discussed by Pearce et al. (2001), Croft et al. (2001), and Springel & Hernquist (2002). The dotted curve in Figure 1 shows the result of correcting the 50 h^{-1} Mpc cube mass function for this effect, using an empirical formula derived from the 22.222 h^{-1} Mpc simulations (M. Fardal et al. 2003, in preparation). This curve represents our best guess at the mass function we would obtain with a 2×288^3 particle simulation of a 50 h^{-1} Mpc cube including a UV background field. With this rescaling, the gap between the SPH and SA mass functions is a roughly constant factor of 3–4. As shown by Weinberg et al. (2002), the weak-lensing mass-to-light ratios obtained from the 50 h^{-1} Mpc simulation (with this rescaling) agree fairly well with those inferred by McKay et al. (2001) from SDSS data. The conflicting implications of the weak-lensing and luminosity function comparisons remain a puzzle, at least if our choice of cosmological parameters is correct.

We select galaxy samples above baryon mass thresholds, but we characterize these samples by their space density $\bar{n}_g$ rather than the mass threshold itself. The membership in a given sample, and thus the HOD, would be unchanged by any monotonic rescaling of galaxy masses. The discrepancy of SA and SPH baryon mass functions reflects the combined impact of differing physical assumptions (e.g., regarding stellar feedback), the approximations in the SA method, and the numerical limitations of the SPH simulation. We

will not attempt to disentangle these contributions here, but we will show that the two approaches nonetheless give similar predictions for the clustering of galaxy samples at common space density.

Figure 2 shows the most commonly studied galaxy-clustering statistic, the two-point correlation function, for the two $\bar{n}_g = 0.02\ h^3$ Mpc^{-3} galaxy samples and for the dark matter in the SPH simulation. We compute the correlation function of SA galaxies by populating the SPH dark matter halos with SA galaxies assuming that, in every halo that contains one or more galaxies, the first galaxy is located at the center of mass of the halo and any remaining galaxies trace the dark matter distribution within the halo. The plotted correlation function of SA galaxies is the mean $\xi_g(r)$ of the 10 SA realizations, and the plotted error bars show the uncertainty in the mean; the 1 σ dispersion from one $P(N|M)$ realization to another is a factor of $10^{1/2}$ larger. The SA error bars therefore illustrate the uncertainty due to fluctuations in $P(N|M)$, but they do not include uncertainty due to the finite number of large-scale structures in the 50 h^{-1} Mpc cube. The SPH error bars, on the other hand, are computed by jackknife resampling using the eight octants of the simulation cube (see Weinberg et al. 2002), and they are dominated by the "cosmic variance" in these large-scale structures. For comparison, we show a power law with the parameters derived for L_* galaxies in the 2dF redshift survey (Norberg et al. 2002a).

The dark matter correlation function shows the steepening at $r \sim 1 \ h^{-1}$ Mpc and leveling off at $r \lesssim 0.3 \ h^{-1}$ Mpc that has been found in most N-body studies (e.g., Jenkins et al. 1998; though the deviation from a power law there is stronger than here because of a larger value of σ_8). Both the SPH and SA models have correlation functions that are closer to a straight power law over the range $r \sim (0.05–2) \ h^{-1}$ Mpc, although, like the dark matter, they show a kink at that larger scale. The difference between the model galaxy and dark matter correlation functions is difficult to see because of the small size of the simulation box. This difference stands out more strongly when we use the SPH and SA HODs to populate a larger volume N-body simulation (shown in Fig. 21). The low amplitude of the model $\xi_g(r)$ at scales larger than $\sim 1 \ h^{-1}$ Mpc compared with the 2dF points in Figure 2 is partly a consequence of the particular realization of structure in this $50 \ h^{-1}$ Mpc volume (Weinberg et al. 2002) and partly due to the fact that our $\bar{n}_g = 0.02$ threshold corresponds to a population of galaxies less luminous than L_*. The comparison of the SPH $\xi_g(r)$ with observations is discussed at greater length by Weinberg et al. (2002). The correlation functions of the two models differ slightly, with the SA model having a higher amplitude of $\xi_g(r)$ on scales smaller than $\sim 0.8 \ h^{-1}$ Mpc and a somewhat more pronounced feature around $\sim 3 \ h^{-1}$ Mpc. From $\xi_g(r)$ alone, it is difficult to say what differences in galaxy formation physics are responsible for these differences in clustering. With the HOD analysis that follows, we will see that the small scale difference arises mainly from the greater representation of galaxies in the highest-mass halos predicted by the SA model.

3. HALO OCCUPATION PROBABILITIES $P(N|M)$

We now turn to the primary results of this study, comparison of the $P(N|M)$ predicted by the SPH and SA models. Unless we specify otherwise, the results we show are for the galaxy samples constructed to have a space density of $\bar{n}_g = 0.02 \ h^3$ Mpc^{-3}, corresponding to galaxies brighter than $\sim 0.2 L_*$ for the Blanton et al. (2001) r-band luminosity function or the Norberg et al. (2002b) b_J-band luminosity function.

Figure 3 shows $N(M)$ predicted by the SPH model (*top*) and a single realization of the SA model (*bottom*). Each point represents the number of galaxies in a specific halo, and the solid curve shows the mean $\langle N \rangle$ and its statistical uncertainty, computed in bins of halo mass. The general features that can be seen in $\langle N \rangle_M$ (we use this notation to denote the mean occupation as a function of halo mass) for both models are a sharp drop in the fraction of halos that contain a galaxy for halos of mass less than $\sim 5 \times 10^{11} \ M_\odot$ and a slope that increases from roughly $\langle N \rangle \propto M^{0.2}$ to $\langle N \rangle \propto M^{0.8}$ as M gets larger. This behavior is similar to that of the broken power law $\langle N \rangle_M$ shown by BW to produce a good match to the observed galaxy correlation function (their Fig. 9). For halos with $M \lesssim 2 \times 10^{12} \ M_\odot$, the distribution $P(N|\langle N \rangle)$ is close to a "nearest integer" (Nint) distribution with only two possible multiplicities, 0 and 1 or 1 and 2.[9] The scatter in $P(N|\langle N \rangle)$ is larger at higher masses—

[9] In Benson et al. 2000b and BW, this is referred to as the "average" distribution, since it is as close as one can come to $N = \langle N \rangle_M$, given that the former is integer valued and the latter is not. The general definition is $p(N_l|\langle N \rangle) = 1 - (\langle N \rangle - N_l)$, $p(N_l + 1|\langle N \rangle) = \langle N \rangle - N_l$, where N_l is the integer satisfying $N_l \le \langle N \rangle < N_l + 1$, with $p(N|\langle N \rangle) = 0$ for all other values of N.
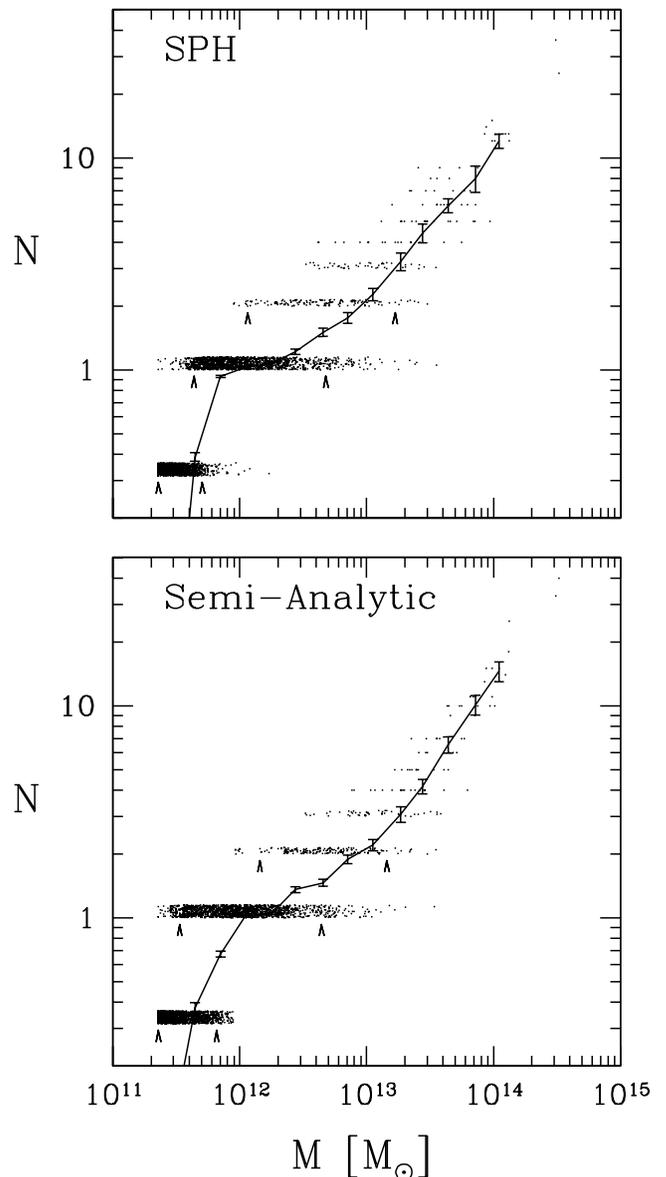

FIG. 3.—Predicted $N(M)$ from the SPH and SA models. Each point represents the number of galaxies above a baryonic mass threshold (selected to yield a galaxy population of space density $\bar{n}_g = 0.02 \ h^3$ Mpc^{-3}) that occupy a single dark matter halo in the SPH simulation (*top*) and a single realization of the SA model (*bottom*). Points for halos that contain no galaxies are arbitrarily placed at $\log N = -0.5$. A small random vertical scatter is added to points with $N < 4$ to reduce saturation, and caret marks indicate the central 90% of points with $N < 3$. The solid curves show the mean $\langle N \rangle$ and its uncertainty, computed in bins of $\log M$.

for example, a $10^{13} \ M_\odot$ halo may have one to four galaxies—but we will show that the scatter remains significantly below that of a Poisson distribution up to $M \sim 2 \times 10^{13} \ M_\odot$. Overall, the results in Figure 3 are in qualitative agreement with results from other hydrodynamic simulations (White et al. 2001; Yoshikawa et al. 2001; Pearce et al. 2001) and semianalytic calculations (Kauffmann et al. 1999; Benson et al. 2000b; Somerville et al. 2001).

3.1. *Mean Halo Occupation*

We compare the $\langle N \rangle_M$ relations predicted by the SPH and SA models in Figure 4. The result for the SA model is the average over the 10 SA realizations, resulting in smaller
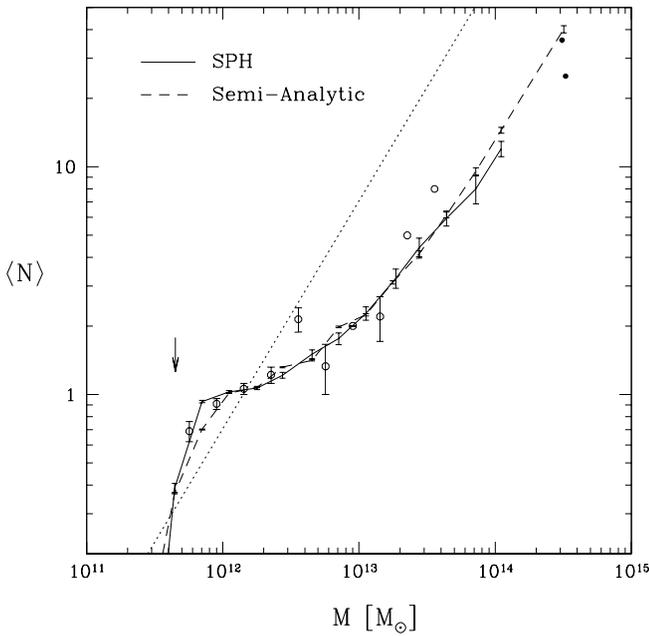
FIG. 4.—Predicted $\langle N \rangle_M$ relation from the SPH and SA models. The curves show the mean $\langle N \rangle$ and its uncertainty, computed in bins of $\log M$, for the SPH (*solid curve*) and SA (*dashed curve*) models. Both models have minimum galaxy baryonic masses selected to yield a galaxy population of space density $\bar{n}_g = 0.02\ h^3\ \mathrm{Mpc}^{-3}$. In the SA case, we use 10 random realizations of each halo, resulting in smaller error bars for $\langle N \rangle_M$. In the SPH case, we show the two most massive halos as points. For purpose of comparison, we show the relation $\langle N \rangle \propto M$ (*dotted line*), normalized so that $N = 1$ at the same mass as the SPH and SA models. The arrow marks the halo mass that would contain a total baryonic mass equal to the minimum SPH galaxy baryonic mass, assuming the universal baryon to mass ratio. Open circles show the $\langle N \rangle_M$ results obtained from a smaller volume simulation with a factor of 8 higher mass resolution. Error bars for these circles are shown only for mass bins that contain at least three halos.

error bars, especially at $M \sim 3 \times 10^{14}\ M_\odot$, for which there are only two halos in the SPH simulation. Also shown is the relation $\langle N \rangle_M \propto M$, normalized so that $N = 1$ at the same mass as the SPH and SA models (*dotted line*). The agreement between the two predicted $\langle N \rangle_M$ relations is strikingly good. They have roughly the same cutoff at low mass and the same shape and amplitude across more than 2 orders of magnitude in halo mass. The only notable differences are that the SPH simulation predicts a slightly sharper cutoff at low masses and slightly fewer galaxies on average in the highest-mass halos, though with a single SPH realization it is not clear that this latter discrepancy is statistically significant. Our matching of number densities requires that the integrals $\bar{n}_g = \int_0^\infty \langle N \rangle_M n(M) dM$, where $n(M)$ is the halo mass function, be equal in the two models, but it clearly does not enforce the detailed agreement seen in Figure 4.

We expect a low-mass cutoff in $\langle N \rangle_M$ simply because lower mass halos do not contain enough gas to form a galaxy of baryonic mass greater than $M_{b,\mathrm{min}}$, the baryonic mass threshold of our sample. If the ratio of galaxy baryonic mass to halo mass were equal to the universal baryon-to-matter ratio, the minimum halo mass would be $M_{\mathrm{min}} = (\Omega_m/\Omega_b) M_{b,\mathrm{min}}$. The vertical arrow in Figure 4 marks this halo mass for the value of $M_{b,\mathrm{min}}$ that defines the SPH galaxy sample. Since this arrow nearly coincides with the sharp drop in $\langle N \rangle_M$, we conclude that many low-mass halos in the SPH simulation cool essentially all the gas within the virial radius

into a single galaxy.[10] The $\langle N \rangle_M$ relation of the SA model also cuts off at this halo mass, but in this case the value of $M_{b,\mathrm{min}}$ is 4 times smaller, implying that these galaxies contain only $\sim 25\%$ of the baryons within the virial radius. As discussed in § 2.3, we attribute this difference to the impact of the stellar feedback parameters in the SA model, which are chosen to match the observed galaxy luminosity function. For the lowest-mass halos in the SA model, feedback results in approximately 4 $M_\odot$ of gas ejected from galaxy disks for every 1 $M_\odot$ of stars formed. Therefore, these halos cool gas with high efficiency, and feedback then determines how much cold gas is allowed to remain in galaxies and form stars. The SA low-mass cutoff is nearly as sharp as the SPH cutoff because the feedback mechanism is tightly correlated with halo mass, so galaxies in SA halos never retain more than $\sim 25\%$ of their gas.

Following the low-mass cutoff, there is a low-occupancy regime ($\langle N \rangle \lesssim 2$) in which the mean number of galaxies rises slowly, growing from one to two over a decade in halo mass. In this regime, halos spend their larger gas supplies on building a more massive galaxy rather than on building multiple low-mass galaxies. Figure 5a demonstrates this point, showing the average baryonic mass $\langle M_b \rangle$ of galaxies in each halo, averaged in bins of halo mass. Although there is a large offset in galaxy mass between the two models, both the SPH and SA models predict a steady increase in $\langle M_b \rangle$ in the low-occupancy regime, leveling off at $M \sim 10^{12.5}$–$10^{13}\ M_\odot$. Continuing to more massive halos, we enter a high-occupancy regime in which $\langle N \rangle_M$ steepens, though the slope remains less than unity except perhaps at the very highest masses. This steepening marks a transition from a regime in which much of the cooling gas is channeled to one or two galaxies to a regime in which halos are built by merging smaller halos whose preexisting galaxies survive, for the most part, as distinct entities. The transition presumably reflects the relative timescales for gas cooling and major halo mergers. A mismatch between the scales of filaments and galaxies in high-mass halos may also play a role in this transition, with filaments of large geometrical cross section no longer able to funnel cooled gas directly onto galaxies (see Katz et al. 2003a). Dynamical friction may also be more effective at bringing together the galaxies of merged halos in the low-mass regime. Figure 5b shows the fraction of total halo mass that is in the form of galaxy baryons, averaged in bins of halo mass. In the high halo mass regime, the efficiency of converting gas to galaxies drops with increasing halo mass, keeping the slope of $\langle N \rangle_M$ below unity. Some of the gas may, of course, be going into galaxies below our mass threshold, rather than not cooling at all.

We can encode these physical ideas in a fitting formula for $\langle N \rangle_M$,

$$\langle N \rangle_M = K \left(\frac{M}{M_{\mathrm{crit}}} \right)^\alpha \left[1 + \left(\frac{M}{M_{\mathrm{crit}}} \right)^\mu \right]^{(\beta - \alpha)/\mu}$$
$$\times \left\{ 1 - \exp\left[-\left(\frac{M}{M_{\mathrm{min}}} \right)^\nu \right] \right\}, \qquad (2)$$

---

[10] We are using the phrase "within the halo virial radius" somewhat loosely here. In the SPH simulation, accretion along filaments means that the Lagrangian (initial) volume of gas within the final virial radius is larger and more irregular than that of the dark matter. Some gas travels long distances along a filament to the central galaxy, while some gas within the halo virial radius remains hot (see Katz et al. 1994, 2003a).
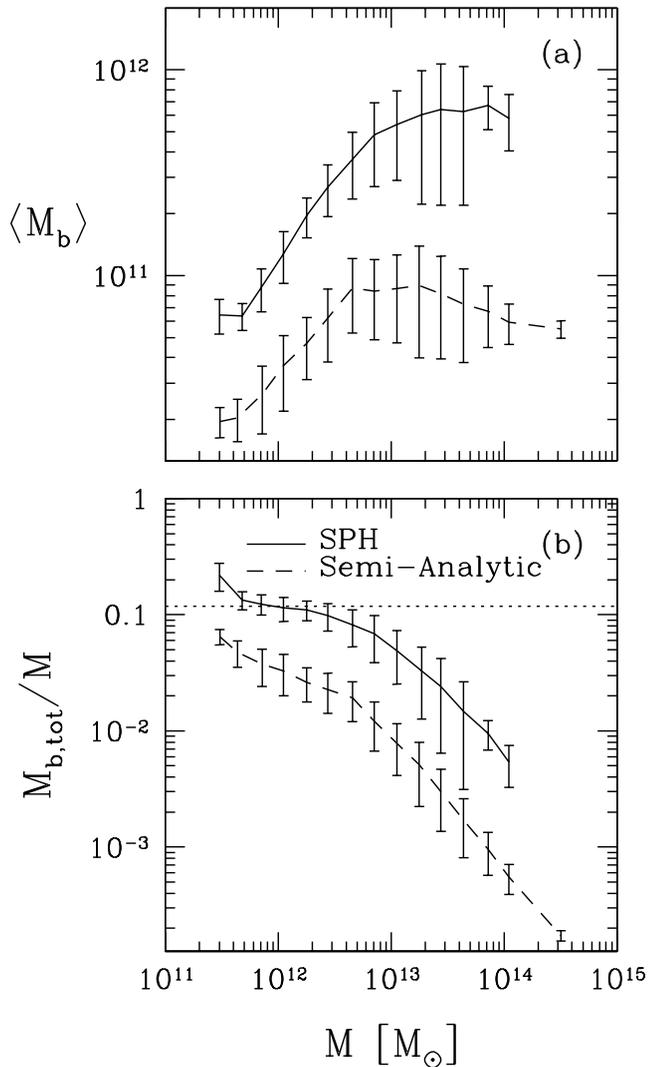
FIG. 5.—(a) Mean baryonic galaxy mass per halo $\langle M_b \rangle$, and (b) fraction of total halo mass contained in galaxy baryons $M_{b,\text{tot}}/M$. The average of these quantities is computed in bins of log M for the SPH (*solid curve*) and SA (*dashed curve*) models. Also shown is the 1 σ scatter in the relations. The dotted line in (b) shows the universal baryon fraction Ω_b/Ω_m. The relation between $\langle M_b \rangle$ and $M_{b,\text{tot}}$ in each halo is simply $M_{b,\text{tot}} = N\langle M_b \rangle$, where N is the number of galaxies in the halo.

which has a cutoff, a low- and high-mass regime, and a transition between them; M_{min} sets the location of the low-mass cutoff, ν determines how sharp it is, α and β are the power-law slopes of $\langle N \rangle_M$ in the low- and high-mass regimes, M_{crit}

is the mass at which the slope changes, and μ determines the speed of the transition. The particular form of the cutoff is chosen because it gives a good match to the numerical results. In place of the normalization constant K, one can specify the mass M_1 of halos that have a mean occupancy of 1, $\langle N \rangle_M = 1$. Table 1 lists the best-fit values of these parameters for the SPH and SA models. The last column in the table lists the maximum logarithmic error of the fitting formula for log$\langle N \rangle$, $\Delta(\log\langle N \rangle)_{\text{max}}$, relative to the numerical results. It is not surprising that we can fit the numerical data with a seven-parameter function, and we could almost certainly find something with fewer parameters that would also work. We choose this form because it seems a natural description of the results and has some basis in the physical interpretation. These fitting functions are useful for boot-strapping the predictions of these models onto larger volume N-body simulations, as we will do in § 6 below.

One natural concern with the SPH predictions is the impact of finite resolution. In particular, one might worry that the effects of dynamical friction are overestimated in low-mass halos and that an excessive galaxy merger rate in this regime could be partly responsible for the very shallow slope of $\langle N \rangle_M$ at low occupancy. Open circles in Figure 4 show the $\langle N \rangle_M$ results obtained from the 22.222 h^{-1} Mpc simulation described in § 2.1. Each halo now has 8 times more dark matter particles than in the 50 h^{-1} Mpc cube, and the baryonic mass threshold now corresponds to the mass of 512 SPH particles rather than 64. While the small volume of the higher resolution simulation leads to poor representation of high-mass halos, the agreement in the low-mass regime is excellent, and the one $M \sim 3 \times 10^{14}~M_\odot$ halo in the small box has similar occupation to those in the large box. The agreement of numerical results across a factor of 8 in mass resolution, as well as the agreement between the SPH and SA results, suggests that the mean occupation function shown in Figure 4 is a secure prediction of the current theory of galaxy formation, given our adopted cosmological parameters.

3.2. *Factorial Moments and* $P(0|M)$

We now turn our attention to higher order moments of $P(N|M)$. These moments influence galaxy clustering on small scales, in which the number of galaxy pairs, triples, and so forth within a single halo becomes important. For example, the two-point correlation function has a one-halo term that depends on the second factorial moment $\langle N(N-1)\rangle_M = \sum_{N=0}^{\infty} N(N-1)P(N|M)$. The three-point correlation function has a one-halo term that depends on

TABLE 1
FIT PARAMETERS FOR $\langle N \rangle_M$ FITTING FUNCTION

$\bar{n}_g$	$M_{b,\text{min}}$	M_{min}	ν	M_{crit}	μ	α	β	M_1	$\langle N \rangle(M_{\text{crit}})$	$\Delta(\log\langle N \rangle)_{\text{max}}$
SPH:										
0.02	10.74	11.70	6.2	12.70	1.6	0.09	0.74	12.00	1.5	0.06
0.01	11.10	12.05	8.2	12.85	5.0	0.21	0.56	12.30	1.4	0.07
0.005	11.38	12.35	7.8	13.40	1.9	0.30	0.70	12.75	1.8	0.14
SA:										
0.02	10.16	11.75	2.9	13.00	1.8	0.22	0.91	12.15	2.0	0.09
0.01	10.50	12.05	2.2	13.15	1.8	0.20	0.81	12.60	1.6	0.07
0.005	10.75	12.35	2.5	13.60	2.0	0.27	0.81	12.90	1.8	0.06

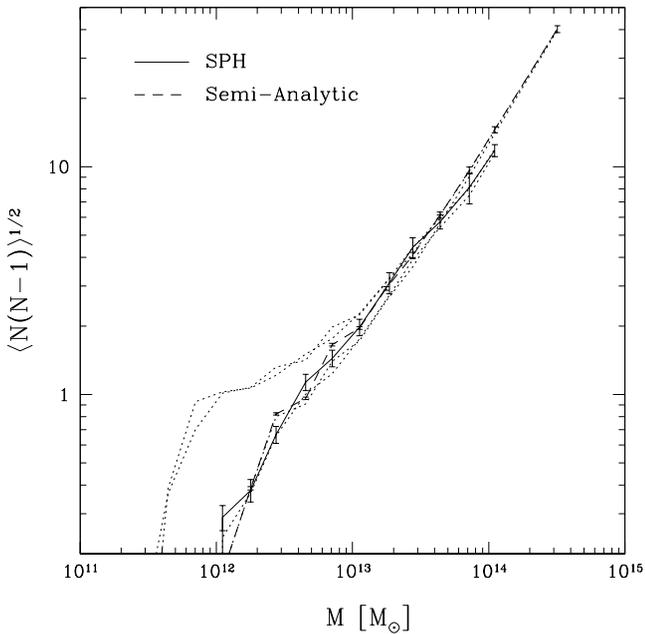NOTE.—Mass columns list $\log(M/M_\odot)$.

FIG. 6.—Predicted $\langle N(N-1)\rangle^{1/2}_M$ relation from the SPH and SA models. The curves show the mean $\langle N(N-1)\rangle^{1/2}$ and its uncertainty, computed in bins of $\log M$, for the SPH (solid curve) and SA (dashed curve) models. Also shown for each model are the bracketing cases of Poisson and nearest-integer $P(N|\langle N\rangle)$ (dotted lines above and below $\langle N(N-1)\rangle^{1/2}_M$, respectively), derived from eqs. (3) and (4).

$\langle N(N-1)(N-2)\rangle_M$ and a two-halo term that depends on $\langle N(N-1)\rangle_M$. Benson et al. (2000b) and BW show that a sub-Poisson $P(N|\langle N\rangle)$ distribution makes it much easier to produce a correlation function of the observed power-law form; the alternative is to put galaxies into halos of implausibly low mass (see also Seljak 2000; Peacock & Smith 2000; Scoccimarro et al. 2001). The $P(N|\langle N\rangle)$ distribution is therefore an important prediction of galaxy formation theories, in addition to $\langle N\rangle_M$.

The solid and dashed lines in Figure 6 show $\langle N(N-1)\rangle^{1/2}_M$, the square root of the mean number of galaxy pairs in halos of mass M, for the SPH and SA calculations, respectively. As in Figure 4, the agreement of the two models is remarkably good. The upper set of dotted curves shows the relation $\langle N(N-1)\rangle^{1/2} = \langle N\rangle$, which would be expected for Poisson $P(N|\langle N\rangle)$ distributions. The lower set of dotted curves shows the corresponding prediction for nearest-integer $P(N|\langle N\rangle)$. Clearly the distributions predicted by the SPH and SA models are much narrower than Poisson distributions when the occupation number is low, and they are close to the maximally narrow Nint distributions. In particular, halos that on average contain zero or one galaxy almost never contain two, and halos that on average contain one or two galaxies rarely contain three (see Fig. 3). Since the cutoff in $\langle N\rangle_M$ at $\langle N\rangle < 1$ is quite sharp, the former result can be understood largely in terms of mass supply: halos with $\langle N\rangle < 1$ do not have enough cold baryons to make two galaxies above the mass threshold. However, $5 \times 10^{12}\ M_\odot$ halos have enough baryonic material to make ~10 galaxies above the SPH baryon mass threshold, and they rarely make even three or four. The sub-Poisson width of $P(N|\langle N\rangle)$ at these scales suggests that halos in this mass regime have a relatively narrow range of formation and accretion histories, a degree of regularity that the SPH and SA calculations evidently agree on.

We can quantify the effects of sub-Poisson fluctuations on halo pair counts via the quantity $\omega = (\langle N^2\rangle - \langle N\rangle^2)/\langle N\rangle$, which is equal to 1 for a Poisson distribution, less than 1 for narrower distributions, and greater than 1 for broader distributions. In terms of this parameter, the second factorial moment is $\langle N(N-1)\rangle = \langle N\rangle^2 + \langle N\rangle(\omega - 1)$. A nearest-integer distribution has $\omega \approx 1$ for $\langle N\rangle \ll 1$, falling to $\omega = 0$ at $\langle N\rangle = 1$. The Nint value of ω is exactly zero at all higher integer values of $\langle N\rangle$, and it rises slightly above zero for noninteger values (Yang et al. 2003).[11] From the mean pair count results plotted in Figure 6, we find that the SPH and SA models predict an ω that falls quickly from 1 to zero in the cutoff regime with $\langle N\rangle < 1$, then rises steadily from zero to 1 as halo masses increase from 10^{12}–$10^{14}\ M_\odot$, with an approximately linear trend of ω with $\log M$. Thus, we find a steady trend from Nint pair counts in the low-occupancy regime to Poisson pair counts in the high-occupancy regime. Note, however, that the fractional difference between Nint and Poisson pair counts is large at low $\langle N\rangle$ but small at high $\langle N\rangle$. One can see from Figure 6 that the Nint model is never very far, in a logarithmic sense, from the predicted pair counts, while the Poisson model is much too high for $\langle N\rangle \lesssim 1.5$. Although we do not show them here, the pair counts predicted by the high-resolution SPH simulation are in good agreement with those predicted by the large-volume simulation.

Figure 7 shows $\langle N(N-1)(N-2)\rangle^{1/3}$, the cube root of the mean number of galaxy triples in halos of mass M. The

----

[11] BW incorrectly implied that the Nint value of ω is zero for all $\langle N\rangle$. A δ-function $P(N|\langle N\rangle)$ has $\omega \equiv 0$, but since a δ-function is not restricted to integer values of N, it is not an acceptable model for this physical situation.
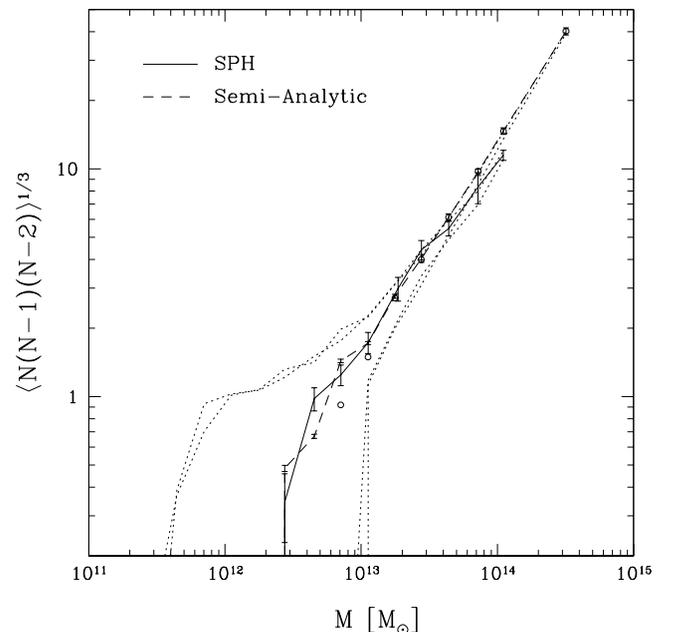

FIG. 7.—Predicted $\langle N(N-1)(N-2)\rangle^{1/3}_M$ relation from the SPH and SA models. The curves show the mean $\langle N(N-1)(N-2)\rangle^{1/3}$ and its uncertainties, computed in bins of $\log M$, for the SPH (solid curve) and SA (dashed curve) models. Also shown for each model are the bracketing cases of Poisson and nearest-integer $P(N|\langle N\rangle)$ (dotted lines above and below $\langle N(N-1)(N-2)\rangle^{1/3}_M$, respectively), derived from eqs. (3) and (4). The open circles show $\langle N\rangle(1 + 3\bar\xi_2)^{1/3}$ for the SA model, where $\bar\xi_2$ is the second-order volume-averaged connected correlation as defined in § 3.2.

SPH and SA predictions, shown by the solid and dashed lines, respectively, again agree very well. A Poisson $P(N|\langle N\rangle)$ has $\langle N(N-1)(N-2)\rangle^{1/3} = \langle N\rangle$, shown by the upper dotted curves in Figure 7. The predicted triple counts are substantially sub-Poisson, though in this case they are higher than those for a nearest-integer distribution shown by the lower dotted curves. It is interesting to examine this behavior in terms analogous to those used in studies of counts-in-cells statistics (e.g., Colombi et al. 2000).[12] We define volume-averaged, connected correlations $\bar{\xi}_2(M)$ and $\bar{\xi}_3(M)$ by the relations

$$\langle N(N-1)\rangle = \langle N\rangle^2 (1+\bar{\xi}_2) ,$$
$$\langle N(N-1)(N-2)\rangle = \langle N\rangle^3 (1+3\bar{\xi}_2 + \bar{\xi}_3) . \quad (3)$$

A Poisson $P(N|\langle N\rangle)$ has $\bar{\xi}_2 = \bar{\xi}_3 = 0$. A Nint distribution with $N_l \le \langle N\rangle < N_l + 1$ has

$$\bar{\xi}_2 = -\frac{N_l(N_l+1)}{\langle N\rangle^2} + \frac{2N_l}{\langle N\rangle} - 1 ,$$

$$\bar{\xi}_3 = -\frac{2N_l(N_l^2-1)}{\langle N\rangle^3} + \frac{6N_l^2}{\langle N\rangle^2} - \frac{6N_l}{\langle N\rangle} + 2 , \quad (4)$$

which reduce to the δ-function values $\bar{\xi}_2 = -1/\langle N\rangle$ and $\bar{\xi}_3 = 2/\langle N\rangle^2$ for integer values of $\langle N\rangle$. We can obtain values of $\bar{\xi}_2(M)$ from the pair counts plotted in Figure 6. Open circles in Figure 7 show $\langle N\rangle (1+3\bar{\xi}_2)^{1/3}$ for the SA model, i.e., the triple counts predicted if we incorporate the measured sub-Poisson behavior of the pair counts but set $\bar{\xi}_3 = 0$. Since these points match the actual triple counts better than either the Poisson prediction or the full Nint prediction with negative $\bar{\xi}_3$, we conclude that the sub-Poisson statistics of galaxy assembly in the SA and SPH models have a direct impact on pair counts in halos but influence triple counts mainly via this indirect impact on pair counts. We have not investigated higher order factorial moments, but the results here suggest the conjecture $\bar{\xi}_N \approx 0$ for $N > 2$.

In low mass density regions of the universe, the halo mass function is shifted to lower masses (e.g., Mo & White 1996), making it less likely that these regions contain massive halos. The question of whether these regions are void of galaxies thus depends on the probability $P(0|M)$ that a halo of mass M contains zero galaxies of a specified class; the void probability itself is high if $P(0|M)$ is high for all halos below the exponential cutoff scale of the shifted mass function (see BW; § 4.3). Therefore, for calculating galaxy void statistics, the HOD property of greatest importance is $P(0|M)$. Solid and dashed curves in Figure 8 show $P(0|M)$ for the SPH and SA models, respectively. The halos with $N = 0$ are in general not empty of galaxies, but the galaxies that they contain are below our baryonic mass threshold $M_{b,\min}$. Both $P(0|M)$ curves drop from 1 to zero over the mass range 2×10^{11}–10^{12} $M_\odot$, corresponding to the rise in $\langle N\rangle_M$ from zero to 1 in Figure 4. The top two dotted curves show the expectations for Poisson statistics, $P(0|M) = \exp(-\langle N\rangle_M)$. Analogous to the factorial moment results, it is clear that the probability of a high-mass halo being empty is far lower than Poisson statistics would imply. In fact, the SPH and SA results are almost perfectly described by the Nint distribution (*bottom two dotted curves*), for which $P(0|M) = \max(1 - \langle N\rangle_M, 0)$; only the low-amplitude ($P \lesssim 0.02$) tail of the

---

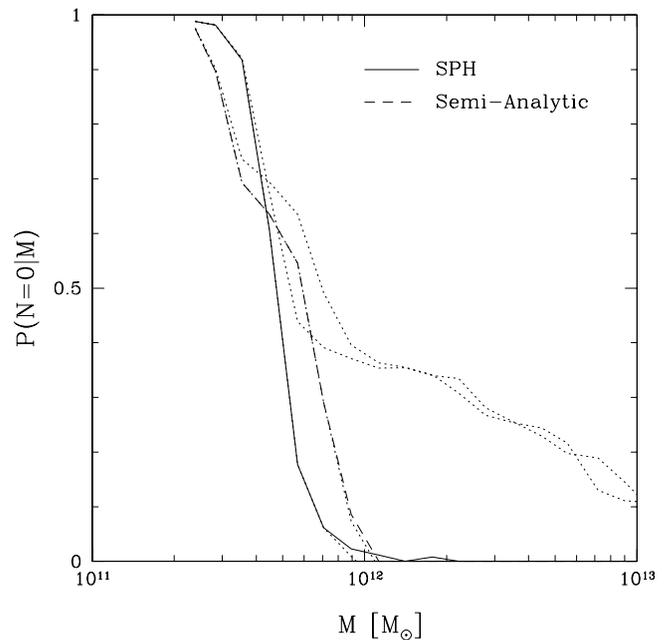[12] We thank S. Colombi and J. Fry for suggesting this analysis.

FIG. 8.—Predicted $P(0|M)$ distribution from the SPH and SA models. The curves show the probability $P(0|M)$ that a halo of mass M contains zero galaxies above the baryonic mass threshold, computed in bins of log M. The top two dotted curves show the expected distributions for a Poisson $P(N|\langle N\rangle)$, which predicts $P(0|M) = \exp(-\langle N\rangle_M)$. The model results are much better described by the nearest-integer prediction $P(0|M) = \max(1 - \langle N\rangle_M, 0)$ [dotted curves that deviate only at the very tail ends of $P(0|M)$].

SPH prediction for 8×10^{11} $M_\odot \lesssim M \lesssim 2 \times 10^{12}$ $M_\odot$ deviates noticeably from this result. The sharpness of $P(0|M)$ is further testimony to the regularity of the galaxy formation process in low-mass halos. In the SPH simulation, halos with $M \lesssim 3.5 \times 10^{11}$ $M_\odot$ almost never contain a galaxy above the baryonic mass threshold, while halos with $M \gtrsim 7 \times 10^{11}$ $M_\odot$ almost always do. The transition is slightly more gradual in the SA model, as one might expect, since the SPH cutoff is driven by the universal baryon fraction while the SA cutoff is determined by the physical processes that suppress gas cooling, whose operation depends to some extent on the halo's formation history. The sub-Poisson nature of $P(0|M)$ slightly decreases the probability of finding large empty voids (see BW; Fig. 14c). However, for galaxy samples defined by luminosity rather than baryonic mass, variations in stellar populations may significantly soften the transition from empty halos to occupied halos.

3.3. *Mass and Age Dependence of $P(N|M)$*

Figure 9 shows $\langle N\rangle_M$ predicted by the SPH and SA models for samples with three different baryon mass thresholds $M_{b,\min}$, with corresponding space densities $\bar{n}_g = 0.02, 0.01$, and 0.005 h^3 Mpc^{-3}. Luminosity-thresholded samples with the same space densities would have $L_{\min} \approx 0.2, 0.45$, and 0.75 L_*, assuming the r-band luminosity function of Blanton et al. (2001) or the b_J-band luminosity function of Norberg et al. (2002b). Not surprisingly, the minimum halo masses are higher for higher baryon mass thresholds, and high-mass halos necessarily contain fewer galaxies above these higher thresholds. The low-mass cutoffs for the SPH
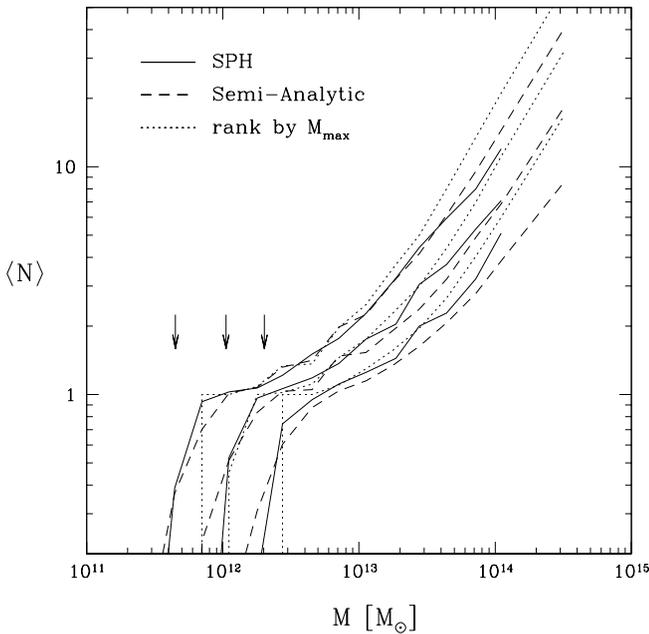
FIG. 9.—Predicted $\langle N \rangle_M$ from the SPH and SA models, as a function of galaxy space density. Both models have minimum galaxy baryonic masses selected to yield galaxy populations of space densities $\bar{n}_g = 0.02 \ h^3$ Mpc^{-3} (*top curves*), 0.01 h^3 Mpc^{-3} (*middle curves*), and 0.005 h^3 Mpc^{-3} (*bottom curves*). The three vertical arrows mark the halo masses that would contain a total baryonic mass equal to the minimum SPH galaxy baryonic mass, under the assumption of a universal baryon to mass ratio. Dotted curves show $\langle N \rangle_M$ for the SA model when galaxies are selected above a threshold in $M_{\max}$ (defined in § 7), rather than their baryonic mass.

$\langle N \rangle_M$ continue to be dictated by the universal baryon fraction, as indicated by the vertical arrows in Figure 9. The SA cutoffs are always somewhat softer than the SPH cutoffs, but they occur at nearly the same halo masses, which is not surprising as it would otherwise be difficult for the two models to have the same galaxy density $\bar{n}_g$.

The striking aspects of Figure 9 are the good agreement between the SPH and SA predictions at all three space densities and the extent to which the change in $\langle N \rangle_M$ is well described by a simple horizontal shift along the log M axis. In terms of the fitting function (eq. [2]), the effect of an increased baryonic mass threshold is, approximately, to multiply the mass scales $M_{\min}$, M_1, and M_{crit} by the ratio f_M of the new and old values of $M_{b,\min}$, while the slopes α and β remain roughly the same. Table 1 lists the values of $M_{b,\min}$ and the fitting function parameters for the different space density samples, and it also lists the values of $\langle N \rangle_M$ at $M = M_{\mathrm{crit}}$, demonstrating that the transition from the low-occupancy regime to the high-occupancy regime occurs at $\langle N \rangle \sim 1.4$–2 in all cases. Figure 10 shows that the good agreement of SPH and SA calculations and the horizontal-shift nature of the dependence on mass threshold also applies to the second factorial moment $\langle N(N-1) \rangle$. We have computed ω for the various samples and find that the transition from Nint to Poisson pair counts always happens at roughly the same mean occupancy. The value of ω typically rises from 0 to 0.5 as $\langle N \rangle$ goes from ~ 1 to ~ 2, and $\omega \approx 1$ for $\langle N \rangle \gtrsim 5$. We have examined lower baryonic mass thresholds in the high-resolution 22.222 h^{-1} Mpc SPH simulation (not shown) and find analogous horizontal shifts of $\langle N \rangle_M$ and $\langle N(N-1) \rangle_M$.
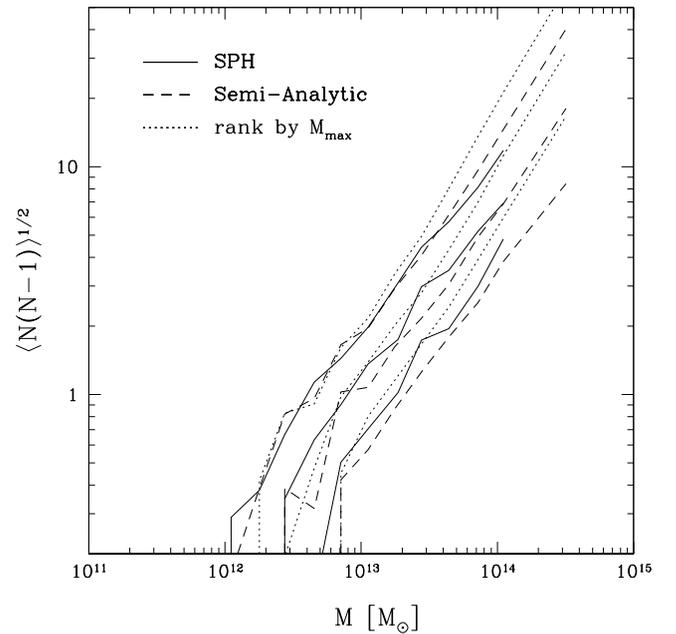

FIG. 10.—Predicted $\langle N(N-1) \rangle_M^{1/2}$ from the SPH and SA models, as a function of galaxy space density. Curves are as in Fig. 9.

Dotted curves in Figures 9 and 10 represent results of a calculation using halo merger tree properties instead of baryonic mass to select SA galaxy samples. We will discuss this calculation in § 7.

The clustering of galaxies is well known to depend on galaxy color or spectral type and on galaxy morphology (see Norberg et al. 2002a; Zehavi et al. 2002, and numerous references therein). Reproducing the observed type dependence of clustering is an important test for theories of galaxy formation. Figure 11 shows the mean occupation $\langle N \rangle_M$ predicted by the SPH and SA models for galaxies in four quartiles of stellar population age, which should correlate tightly with color or spectral type. The SPH ages are median mass-weighted stellar ages, while the SA ages are mean mass-weighted stellar ages, because these quantities are straightforward to compute in the two analysis codes. Although there are differences between the SPH and SA predictions in individual age quartiles, the agreement on the qualitative dependence of $\langle N \rangle_M$ on galaxy age is remarkably good. Old galaxies have a steep $\langle N \rangle_M$ relation, with most galaxies occupying high-multiplicity halos, whereas young galaxies have a shallow $\langle N \rangle_M$ and reside primarily in single-galaxy halos. In the language more commonly used to describe the environmental dependence of galaxy types, both calculations predict that old, red, or early-type galaxies reside preferentially in clusters and that young, blue, or late-type galaxies reside mainly in the field. This result emerges from two aspects of the galaxy formation physics. First, gravitational collapse and galaxy assembly begin earlier in the overdense regions that eventually form massive halos. Second, gas accretion largely shuts off when a galaxy's parent halo merges into a more massive halo, starving the galaxy of the fuel that it would need to make young stars. The galaxies that are in high-mass halos today started forming their stars early, and they stopped forming them some time ago.

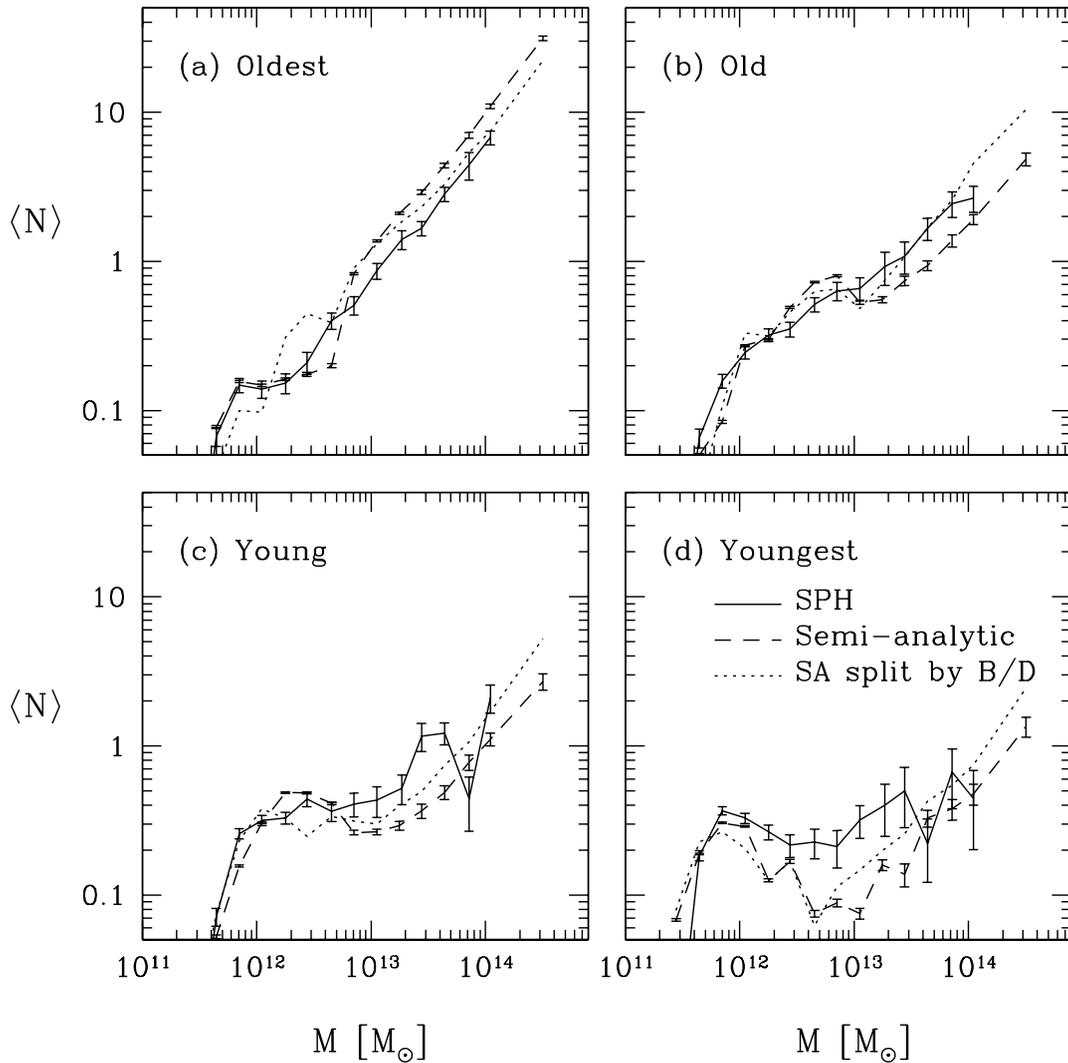The SPH simulation does not resolve galaxy morphology, but the SA model does track morphology, assigning

FIG. 11.—Dependence of $\langle N \rangle_M$ on galaxy age. The four panels correspond to four age quartiles for the $\bar{n}_g = 0.02\ h^3$ Mpc^{-3} samples, from oldest (a) to youngest (d). In each panel, solid and dashed curves show results for SPH and SA galaxies, respectively, with error bars showing the error on the mean in each mass bin. Dotted curves show SA galaxies classified into quartiles based on their bulge-to-disk ratio, from bulge dominated (a) to disk dominated (d).

postmerger stellar populations to bulge components as described in § 2.2. Galaxy color and morphological type are correlated with environment in similar ways. Nonetheless, the physics that determines morphology is different from the physics that governs stellar population age, and it is interesting to ask whether the SA model predicts a morphological dependence of clustering that is distinguishable from the age dependence. Dotted curves in Figure 11 show the SA predictions for galaxy quartiles defined by bulge-to-disk ratios (in stellar mass) rather than by stellar population age. While there is a fair amount of galaxy-by-galaxy scatter between mean stellar age and bulge-to-disk ratio, the two ways of characterizing galaxy type display similar mean occupation functions. The SA model thus predicts that the morphological dependence of clustering will closely track the age dependence of clustering.

Closer inspection of Figure 11 reveals interesting structure in the SA $\langle N \rangle_M$ curves that is significant relative to the error bars. For the youngest quartile, $\langle N \rangle_M$ has a maximum at $M \approx 10^{12}\ M_\odot$, then falls before rising again at $M \gtrsim 10^{13}$ $M_\odot$. The next two quartiles show similar peaks in $\langle N \rangle_M$, at

$M \approx 3 \times 10^{12}$ and $M \approx 8 \times 10^{12}\ M_\odot$. These peaks represent the contribution of the halos' central galaxies, the ages of which are correlated with the halo masses. Young central galaxies form in low-mass halos, and the mean occupation for these galaxies declines toward higher halo mass as the central galaxy age moves out of the youngest quartile and into the second quartile, and so on for the third. The oldest quartile has a very low plateau for low halo masses because the galaxies of these halos are almost always younger; then there is a sharp rise when the halo mass gets high enough that central galaxies can be in the oldest quartile. A similar peak at low halo masses for young or blue galaxies is also seen in the GIF semianalytic models of Kauffmann et al. (1999), and it is modeled as a Gaussian bump by Sheth et al. (2001a) and Scranton (2002). While the behavior of the SPH $\langle N \rangle_M$ curves is similar, the structure is much less pronounced, indicating that the SPH calculation produces more scatter between halo mass and central galaxy age. Some of this difference could arise from the different age definitions, though there is no obvious reason that median ages would exhibit more scatter than mean ages. The
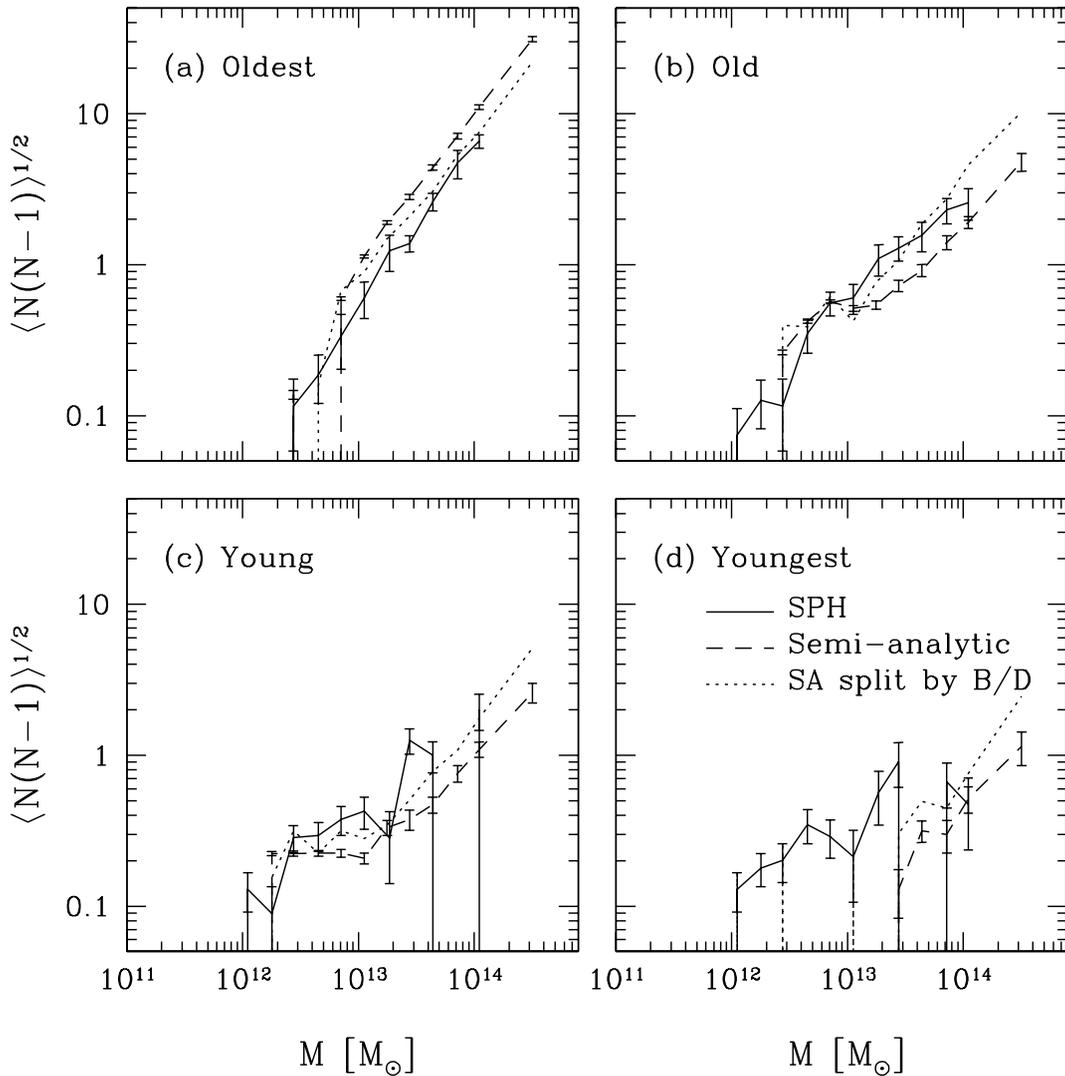
FIG. 12.—Dependence of $\langle N(N-1)\rangle_M^{1/2}$ on galaxy age and (for the SA model) bulge-to-disk ratio. Panels and curves are as in Fig. 11.

existence of local maxima in $\langle N \rangle_M$ means that our fitting formula (2) does not describe the age quartile results accurately, so we do not attempt to perform fits for these samples.

Figure 12 shows that the SPH and SA models predict qualitatively similar pair counts $\langle N(N-1)\rangle_M$ for the age quartiles, though the results are fairly noisy. As with the mean occupation, age and bulge-to-disk divisions produce similar results for the SA model. Overall, the strong age dependence of $P(N|M)$ implies that both SPH simulations and SA models predict a strong dependence of galaxy clustering on stellar population age. The similarity of the predicted trends indicates that for all clustering statistics these dependences will be similar for the two methods.

Figure 13 (top) shows the mean occupation for young, old, and all galaxies in the SPH and SA models, when the $\bar{n}_g = 0.02 \; h^3 \; \mathrm{Mpc}^{-3}$ sample is divided into two halves according to age. While the quartile division demonstrates the steadiness of trends with age, this division in two yields more statistically robust predictions that can be tested against, for example, the red and blue halves of a volume-limited galaxy sample. For both the SPH and SA calculations, the mean occupation of older galaxies is close to a power law truncated at M_{min}, and the slowly rising regime

of the total $\langle N \rangle_M$ curve comes from adding this power law to the much flatter occupation curve of young galaxies. The SA model predicts that in the high halo mass regime ($M \gtrsim 10^{13} \; M_\odot$), the power-law slope of $\langle N \rangle_M$ for both old and young galaxies is equal to that of $\langle N \rangle_M$ for all galaxies. This suggests that the fraction of young to old galaxies is constant in this regime. This behavior is seen in Figure 13b (bottom), which shows the fraction of young galaxies in halos as a function of halo mass. The SA model predicts that the young fraction drops steadily from 90% to 10% as halo mass increases from the minimum cutoff mass to $\sim 10^{13} \; M_\odot$ and then levels off at 10% for greater masses. The SPH model prediction for the young fraction (Fig. 13a, bottom) shows no clear evidence for this high-mass plateau, but it is too noisy to tell for sure. The mass dependence of the SA young fraction differs from that of the "late-type fraction" parameterization assumed by van den Bosch et al. (2003), which is forced to zero at high halo masses.

3.4. (No) Environmental Dependence of $P(N|M)$

The claim that the HOD formalism offers a complete description of galaxy bias hinges on a key assumption: if we
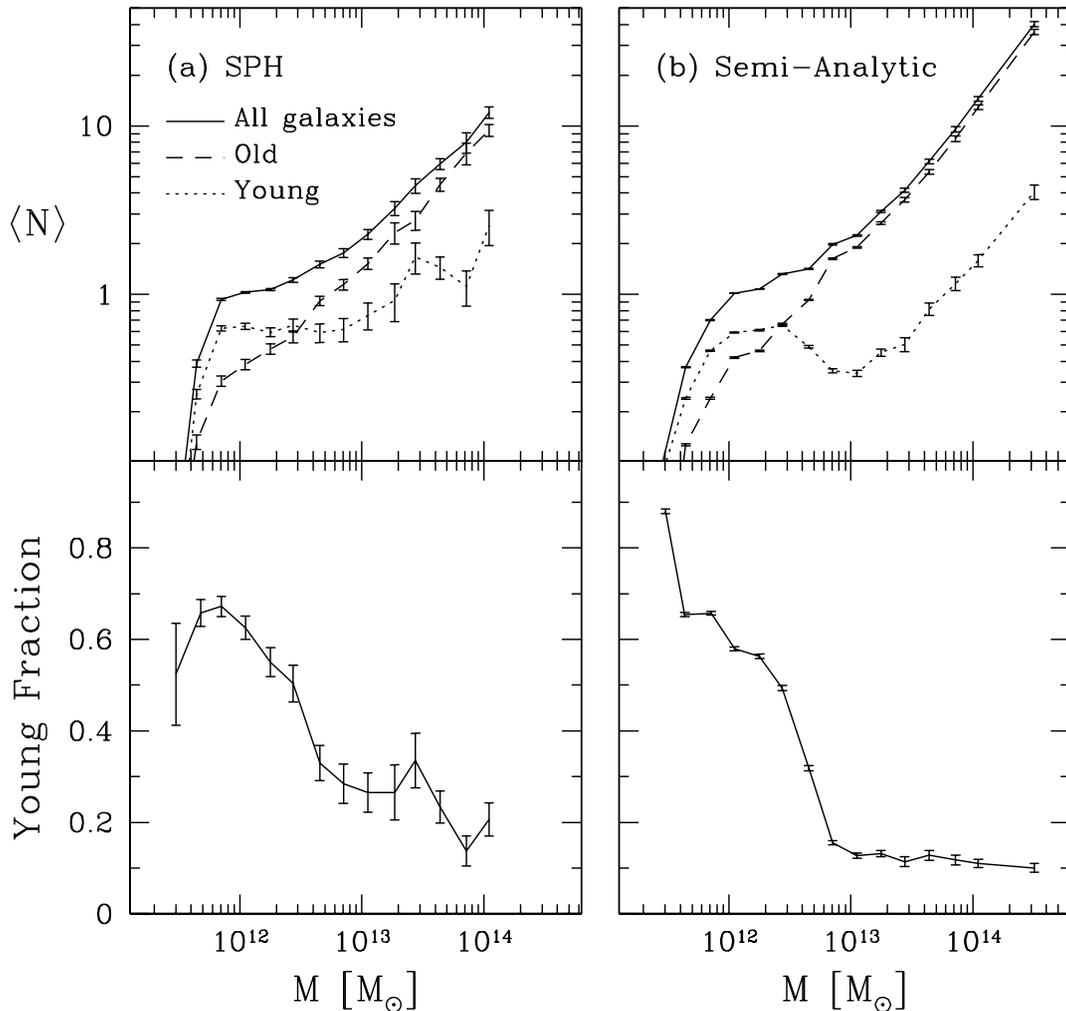
FIG. 13.—Fraction of young galaxies as a function of halo mass. *Top*, Mean halo occupation of old (*dashed curves*), young (*dotted curves*), and all (*solid curves*) galaxies in the (*a*) SPH and (*b*) SA models, when the $\bar{n}_g = 0.02\ h^3$ Mpc^{-3} sample is divided into two equal halves according to age; *bottom*, mean fraction of young galaxies in halos as a function of halo mass. Error bars show the uncertainty in the mean, calculated in halo mass bins.

know, statistically, how galaxies occupy halos of given mass, then we can predict all aspects of galaxy clustering given a halo population. This assumption would break down if halos of the same mass in different large-scale environments had systematically different galaxy populations. The excursion set model (Bond et al. 1991) predicts that the statistics of a halo's progenitor population and merger history depend only on its mass, not on its environment. The SA model employed here is on based on excursion set merger trees, so it necessarily incorporates no direct dependence of galaxy population on halo environment. The analysis of *N*-body simulations by Lemson & Kauffmann (1999) shows that halos of the same mass in different environments have similar properties and formation histories, providing substantial support for this approach. Nonetheless, it is desirable to revisit this central issue with a simulation that includes the gas dynamics and dissipation that play key roles in galaxy formation.

Figure 14 shows $\langle N \rangle_M$ for the SPH galaxy populations of halos in different bins of large-scale density. The density around each halo is found by smoothing the dark matter distribution with a top-hat filter of radius 4 h^{-1} Mpc. As expected, the low-density bins probe only $\langle N \rangle_M$ in the low halo mass regime, and successively higher density bins

probe $\langle N \rangle_M$ to higher masses, demonstrating the expected shift of the halo mass function with environment (see Mo & White 1996). The main result, however, is unambiguous: the mean halo occupation of galaxies is completely independent of the larger scale environment. The same is true for $\langle N(N-1) \rangle_M$, although we do not plot that result here. We thus conclude that, to the extent that the SPH simulation includes the most important macroscopic galaxy formation physics, the claim that the HOD is a complete formulation of galaxy bias is well founded. The large-scale relative bias between early and late type galaxies, predicted by both the SA and SPH approaches (Benson et al. 2000a; Weinberg et al. 2002), arises entirely from the dependence of the halo mass function on the large-scale environment, not from changes in galaxy populations at fixed halo mass.

4. DISTRIBUTION OF SPH GALAXIES WITHIN HALOS

In this section we investigate the second component of the HOD: the relative spatial and velocity distributions of galaxies and dark matter within halos. The spatial bias of galaxies within halos has a more limited impact on galaxy clustering than $P(N|M)$ because its effect is restricted to
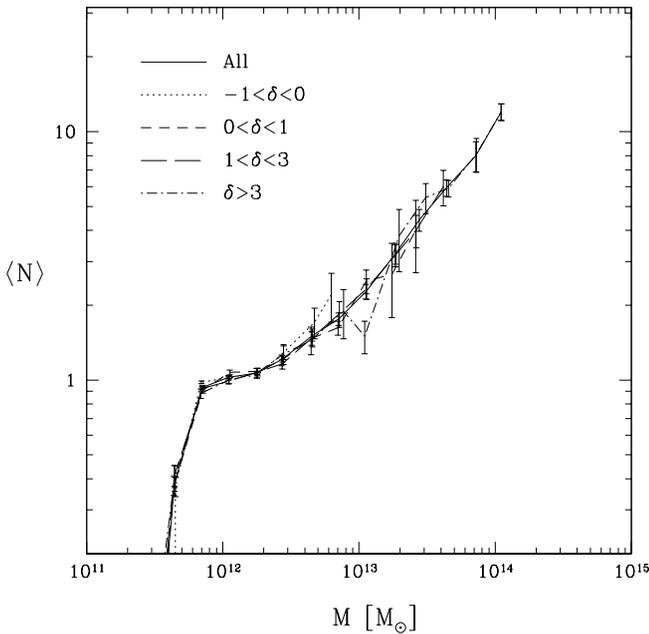
FIG. 14.—Environmental dependence of $\langle N \rangle_M$ in the SPH model. $\langle N \rangle_M$ and its uncertainty is shown for all halos (*solid curve*) and for halos in four bins of dark matter density contrast, δ, as marked, where δ is computed in top-hat spheres of radius 4 h^{-1} Mpc around each halo. While the distribution of halo masses shifts with δ, there is no discernible dependence of the galaxy occupation at fixed M on the larger scale environment.

scales smaller than halo virial diameters. Nevertheless, internal spatial biases can have an important effect on small-scale clustering, such as the correlation function at separations $r \lesssim 0.3\ h^{-1}$ Mpc (BW; Fig. 6). Systematic differences between galaxy and dark matter velocity dispersions within halos, namely, velocity bias, can have a major impact on redshift space clustering even at very large scales (BW; Figs. 15 and 16). While the SA model treats presumed central galaxies differently from satellites, it does not directly predict spatial or velocity distributions within halos. Clustering predictions based on the combination of SA modeling with N-body simulations often assume that the central galaxy resides at the halo center of mass and moves with the halo center of mass velocity and that satellites trace the dark matter spatial and velocity distribution (e.g., Kauffmann et al. 1997; Benson et al. 2000a, 2000b). Kauffmann et al. (1999) adopt a somewhat different procedure, in which satellite galaxies trace the most bound particle of their parent halo, leaving some internal bias (Diaferio et al. 1999). In the SPH simulation, we can investigate internal biases in a calculation that includes the full effects of gas dynamics, dynamical friction, and galaxy mergers.

Figure 15a plots the distribution $r_{\rm cen}/R_{\rm vir}$ versus M, where $R_{\rm vir}$ is the halo virial radius and $r_{\rm cen}$ is the distance from the halo center of mass to the galaxy that is closest to it. Each point represents an individual halo. The central solid curve shows the mean $r_{\rm cen}/R_{\rm vir}$ in mass bins, and the upper and lower solid curves enclose 60% of the points. On average, the centermost galaxy of a halo resides within $0.1R_{\rm vir}$ of the halo center of mass. To obtain corresponding predictions for the case in which galaxies trace mass within halos, we randomly select from each halo a number of dark matter particles equal to the number of galaxies N. We tag the selected particle closest to the center of mass as the "placebo" particle, and we repeat the process several times
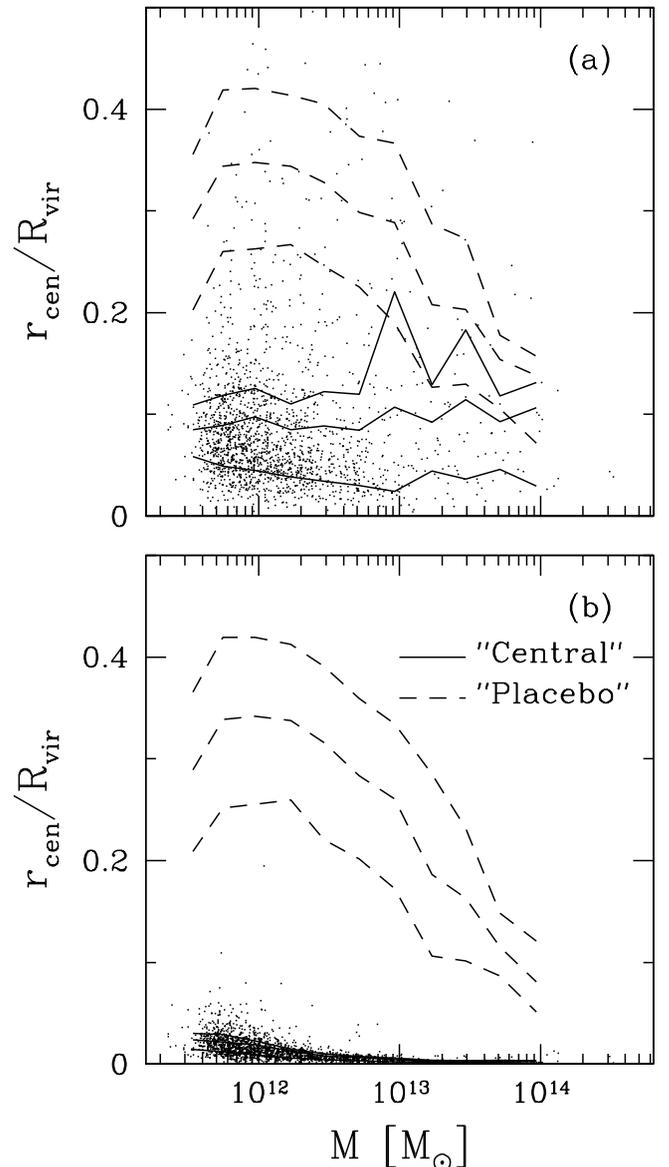

FIG. 15.—(*a*) Distribution of distances of "central" SPH galaxies from their halo centers. In each halo, the SPH galaxy closest to the halo's center of mass is tagged as the "central" galaxy. Each point shows the distance of a central galaxy from its host halo's center of mass, in units of the halo's virial radius. The middle solid curve shows the mean distance in bins of halo mass, and the outer two solid curves enclose 60% of all SPH central galaxies. The dashed curves show the same for dark matter "placebo" particles, which represent the distribution of $r_{\rm cen}/R_{\rm vir}$ that would be expected if SPH galaxies had the same distribution as dark matter within halos. (*b*) Same as (*a*), but with the halo center identified as the position of the most bound dark matter particle instead of the center of mass.

to improve statistics. Dashed curves in Figure 15a mark the mean and central 60% of the distributions of $r_{\rm pcb}/R_{\rm vir}$ in bins of halo mass. Comparison with the solid curves demonstrates that the centermost galaxies in the SPH halos are indeed a distinct, "central" population, whose proximity to the center of mass would not be expected if galaxies randomly traced the dark matter.

The distinction between central galaxies and placebo particles is less clear at large M, but in these high-mass halos, substructure near the virial radius may shift the center of mass position. The location of the most bound dark matter particle or a local density maximum provides a more
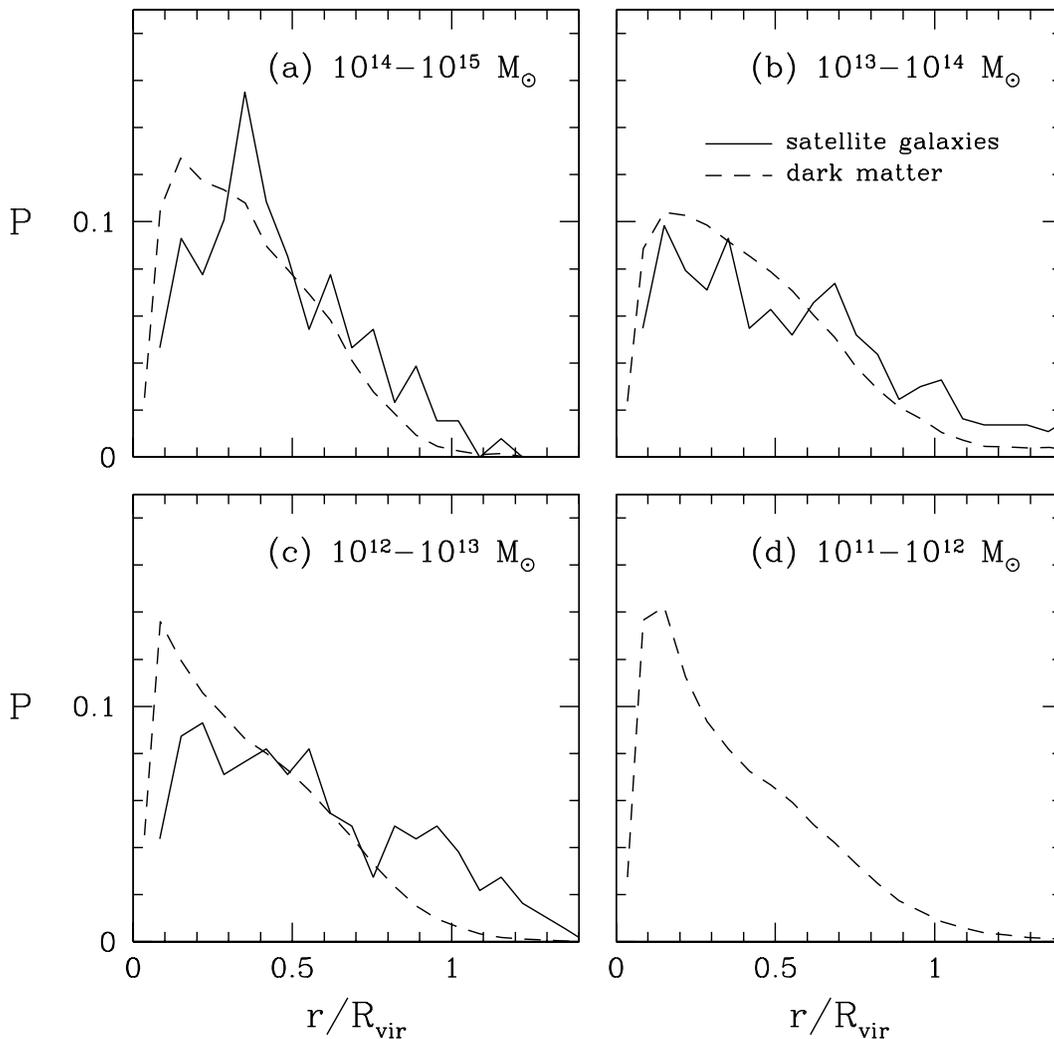
FIG. 16.—Radial distribution of SPH "satellite" galaxies and dark matter within dark matter halos, in four halo mass bins, showing galaxies (*solid curves*) and dark matter (*dashed curves*) Satellites are all galaxies in each halo other than the central galaxy. Halos in the lowest-mass bin never have more than one galaxy, so by definition they do not contain satellite galaxies.

physically robust indicator of the halo center. However, we began with the center-of-mass definition because the most bound dark matter particle is almost guaranteed to lie near the center of a massive galaxy, and with this definition of the halo center one might erroneously infer the existence of "central" galaxies even if galaxies traced the overall dark matter distribution within halos. Figure 15b is the same as Figure 15a except that the halo center is identified as the position of the most bound dark matter particle (specifically, the particle with the lowest potential energy, computed using the halo's dark matter particles only) instead of the center of mass. For the great majority of halos, this particle lies within $0.1R_{vir}$ of the center of mass. As expected, the r_{cen}/R_{vir} distribution is much narrower with the most-bound–particle definition of halo center, while the r_{pcb}/R_{vir} distribution is hardly changed. Since Figure 15a convincingly establishes the existence of central galaxies, we will henceforth use the more reliable most-bound–particle definition to identify which galaxies are central.

What about satellite (i.e., noncentral) galaxies? Figure 16 compares the radial profiles of satellite galaxies (*solid curves*) with those of dark matter (*dashed curves*), in four halo mass

bins. Here we define profiles as the fraction of objects in bins of r/R_{vir}. In all cases, the radial distribution of satellite galaxies traces that of dark matter within halos fairly well. However, there is marginal evidence of a central core in the galaxy distribution relative to that of the dark matter. There are no satellite galaxies in the lowest halo mass bin (d) because these halos never have more than one galaxy.

We now consider the relative velocities of galaxies and dark matter within halos. For every SPH galaxy, we measure $|v_g - v_h|$, the magnitude of its velocity relative to the halo center-of-mass velocity. We then average these measurements in bins of r/R_{vir}, where r is the galaxy's distance from the halo center (most bound particle). We do the same for all dark matter particles. Dividing these two functions gives the "velocity bias" parameter $\alpha_v = \langle|v_m - v_h|\rangle / \langle|v_m - v_h|\rangle$ as a function of radius within halos, similar to the α_v parameter defined by BW (which was assumed to be constant with radius). If galaxies have the same distribution of velocities as random dark matter particles, then $\alpha_v = 1$, while if all galaxies move at their halo's mean velocity, then $\alpha_v = 0$. Figure 17 shows α_v for central (*filled circles*) and satellite (*open circles*) SPH galaxies as a function of r/R_{vir},

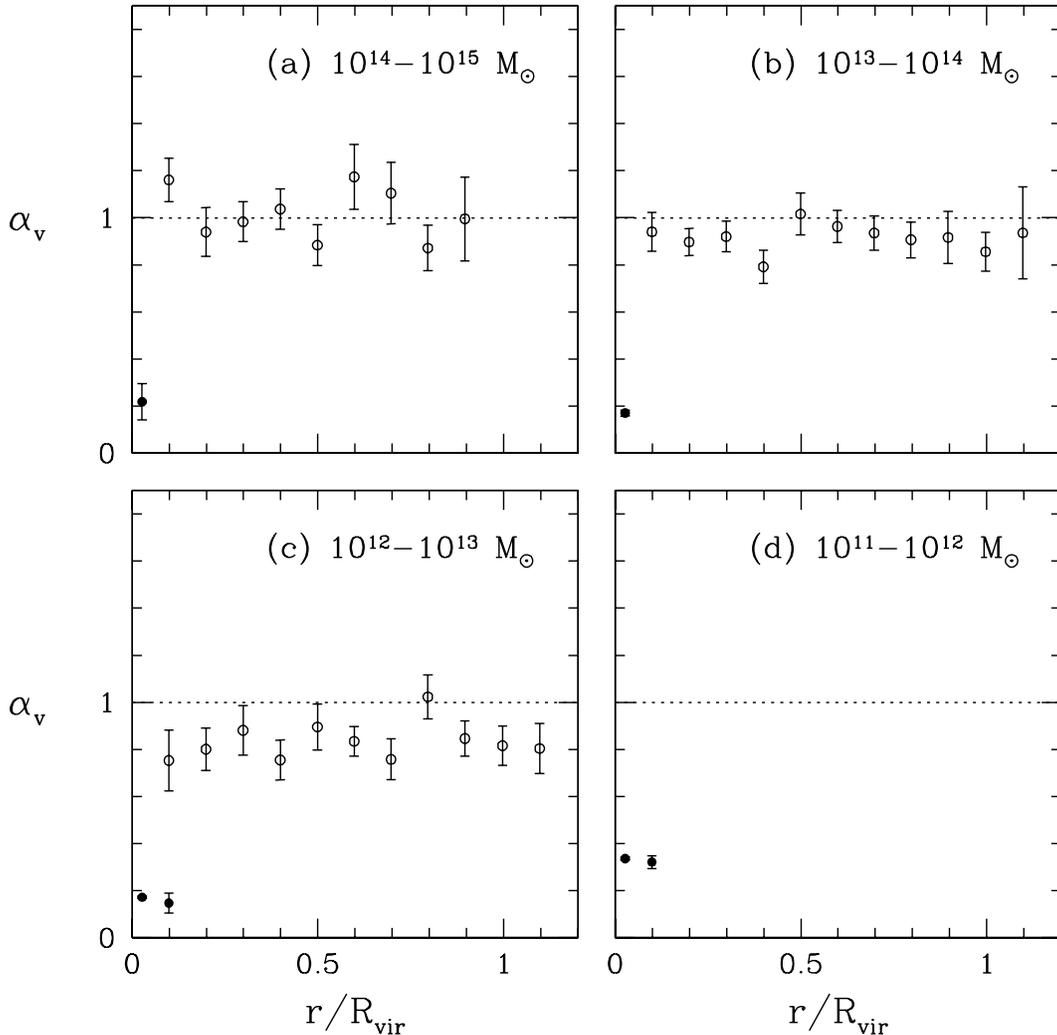Fig. 17.—Velocity bias factor $\alpha_v = \langle|\boldsymbol{v}_g - \boldsymbol{v}_h|\rangle / \langle|\boldsymbol{v}_m - \boldsymbol{v}_h|\rangle$ as a function of radius, in four halo mass bins, showing central galaxies (*filled circles*) and satellite galaxies (*open circles*), with the uncertainty of the mean (*error bars*). The value $\alpha_v = 1$, corresponding to no velocity bias, is marked by the dotted line.

in four halo mass bins. Error bars show the uncertainty in the mean α_v. Central galaxies have velocities that are substantially colder than the dark matter, as expected—if they did not, then they would not remain close to the center. Note that if the central galaxy is identified with the most bound dark matter particle, its velocity should still be set to the center-of-mass velocity; this difference can have an important effect on velocity dispersion statistics (Benson et al. 2000a). To a good approximation, satellite galaxies trace the dark matter velocity distribution, though they exhibit a mild velocity bias $\alpha_v \sim 0.8$–0.9 in 10^{12}–10^{13} $M_\odot$ halos and $\alpha_v \sim 0.9$–0.95 in 10^{13}–10^{14} $M_\odot$ halos.

Overall, the SPH simulation supports a simple characterization of the galaxy distributions within halos: there is always one galaxy at the center of each halo (defined by the center of mass or, better, by the location of the most bound dark matter particle) that moves at approximately the center-of-mass velocity, and any remaining satellite galaxies trace the spatial and velocity distribution of the dark matter. This is just the characterization that has been used for most calculations of galaxy clustering from SA/N-body models, and the only amendment that our SPH results suggest is a mild velocity bias of satellites in intermediate-mass halos

and perhaps a small central core in the galaxy distribution. Here we have presented results for the whole $\bar{n}_g = 0.02$ h^3 Mpc^{-3} sample, but we find that these results also hold for the lower space density samples. However, when we split the whole sample into two halves according to stellar population age, we find that young satellite galaxies have a slightly bigger central core than old satellite galaxies. We find no clear difference between the velocity bias of young and old galaxies.

5. "CENTRAL" VERSUS "SATELLITE" GALAXIES

Having established that SPH halos contain central galaxies, we can compare the properties of central and satellite galaxies in the SPH and SA models. Figure 18 shows the distribution of baryonic masses for central (*top*) and satellite (*bottom*) galaxies. Each point shows M_b for an SPH galaxy versus its host halo mass. The middle solid curves show the mean M_b computed in bins of halo mass, and the outer solid curves enclose 60% of central/satellite SPH galaxies. Dashed curves are similar to solid ones, but for SA central (*top*) and satellite (*bottom*) galaxies. Both models predict a tight correlation between central galaxy mass and host halo
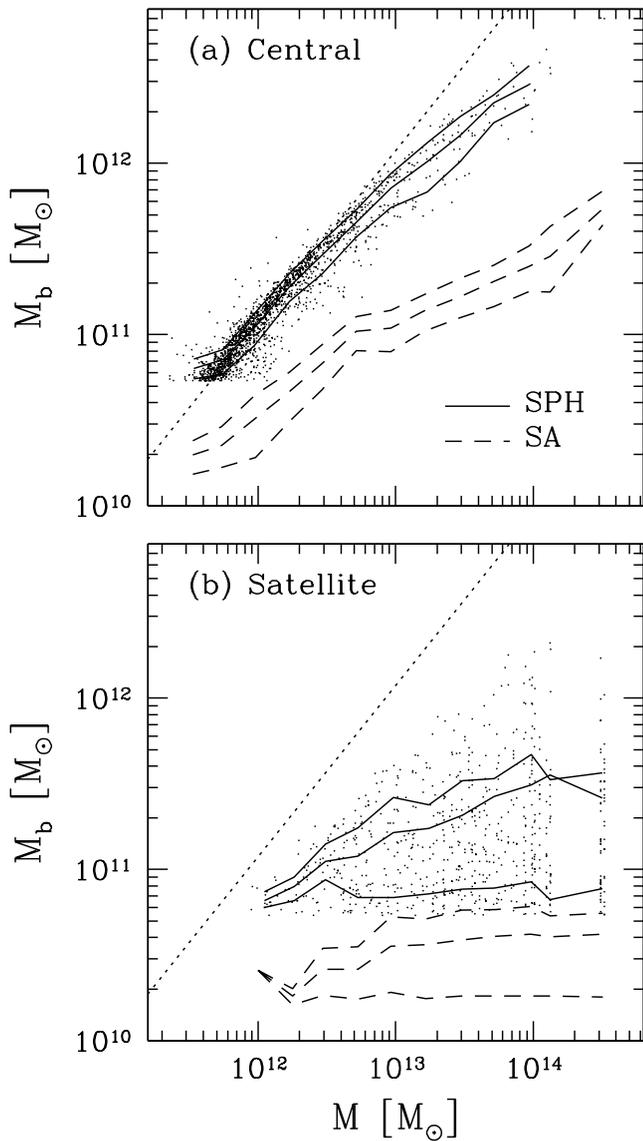
occur when substructure puts the center of mass closer to a low-mass satellite.

As we have already seen in § 2.3, the SPH simulation predicts much higher galaxy masses than the SA model. For $M \lesssim 3 \times 10^{12} \ M_\odot$, the baryonic mass of a typical SPH central galaxy is close to the halo mass multiplied by the universal baryon fraction (*dotted line*). Some galaxies in this regime lie above the dotted line, indicating that they have accreted some gas from beyond the virial volume represented by the friends-of-friends halo. At high M_b, SPH galaxy masses are probably overestimated because of the resolution effects discussed in § 2.3. Correcting for this effect would make little difference to central galaxies at low M, but it would produce a sharper turnover in the trend of M_b
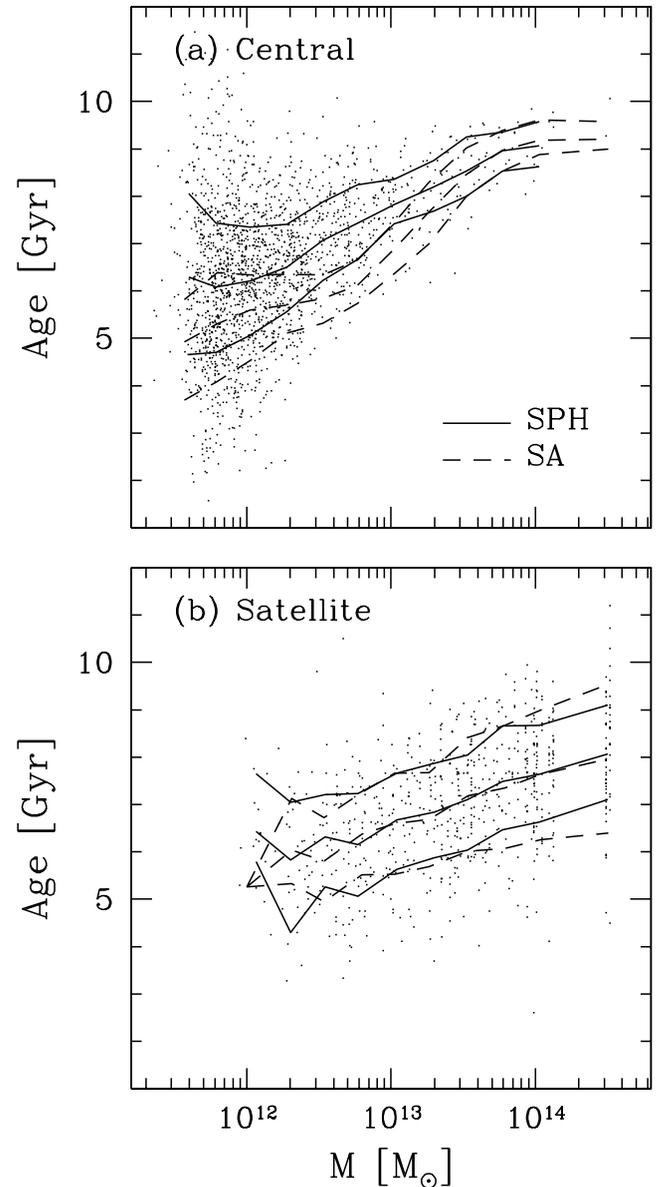

FIG. 18.—Baryonic masses of (*a*) central and (*b*) satellite galaxies vs. their host halo masses. Each point represents the baryonic mass M_b of an SPH galaxy. The middle solid curve shows the mean SPH M_b in bins of halo mass, and the outer two solid curves enclose 60% of all SPH central or satellite galaxies. The dashed curves show the same for (*a*) central and (*b*) satellite SA galaxies. For comparison, dotted lines show the baryonic mass corresponding to the universal baryon fraction, $M_b = (\Omega_b/\Omega_m)M$.

mass. Satellite galaxy masses, on the other hand, are only weakly correlated with host halo masses, especially in the SA model. Furthermore, both models predict that central galaxies are substantially more massive than their satellites and that this difference increases with halo mass. This qualitative behavior is expected in a scenario in which the galaxies at the centers of large halos grow by accreting smaller galaxies. Central galaxies are also better positioned to accrete cooling gas, since they lie at the maximum of the gas density profile; in the SA model, it is assumed that central galaxies accrete gas but satellite galaxies do not. Our definition of SPH halo centers as the locations of the most bound dark matter particles tends to favor high masses for "central" galaxies on its own, but Figure 18 does not look very different if we use a center-of-mass definition instead, though in this case there are some outliers at high M, which

FIG. 19.—Stellar ages of (*a*) central and (*b*) satellite galaxies vs. their host halo masses. Each point represents the median mass-weighted stellar age of an SPH galaxy. The middle solid curve shows the mean SPH galaxy age in bins of halo mass, and the outer two solid curves enclose 60% of all SPH central or satellite galaxies. The dashed curves show the same for the mean mass-weighted stellar ages of (*a*) central and (*b*) satellite SA galaxies.

versus M at high M, making the gap between the SPH and SA predictions roughly independent of halo mass.

Figure 19 shows the distribution of stellar ages for central (*top*) and satellite (*bottom*) galaxies, in a format similar to Figure 18. Both models predict a clear correlation of central galaxy age with halo mass. Satellite galaxy ages also correlate with M, but not as strongly. As previously discussed in § 3.3, these trends reflect the earlier onset of structure formation in regions that become high-mass halos and the decline of gas accretion rates for galaxies that reside in halos of high circular velocity. The age scales in the SPH and SA calculations agree reasonably well, though since they represent median ages for SPH galaxies and mean ages for SA galaxies we would not expect perfect agreement in any case.

Figures 18 and 19 show that central galaxies are generally more massive and older than average satellites in the same halo. Figure 20 addresses a related but distinct question: Is

the central galaxy the most massive and oldest galaxy in the halo? Figure 20 (*top*) shows $\Delta \log M_b$, the logarithmic difference in mass between the central galaxy and the most massive noncentral galaxy in the halo. Figure 20 (*bottom*) shows the age difference between the central galaxy and the oldest noncentral galaxy. Points show individual SPH halos, and solid and dashed curves show mean results in bins of halo mass for the SPH and SA models, respectively. The central galaxy is consistently the most massive galaxy in the halo, with both models predicting an average offset of 0.4–0.6 dex in halos with $M \gtrsim 10^{13} M_\odot$. The decline in $\Delta \log M_b$ at lower M is partly enforced by our baryonic mass threshold, since halos that have only one galaxy above the threshold (and "satellites" below it) do not make it onto the plot. The SPH central galaxies are frequently the oldest in the halo, but the oldest satellite is only slightly younger on average, and sometimes it is older. The SA model predicts little mean age difference between the central galaxy and the oldest satellite. In the most massive halos, the central galaxy is younger than the oldest satellite, presumably because it continues to accrete gas and form stars. At a qualitative level, the predictions of both models are consistent with the fact that observed central galaxies in massive groups and clusters are usually luminous elliptical or cD galaxies.

6. PREDICTIONS FOR THE AUTOCORRELATION FUNCTION

BW showed that, in the context of HOD models of galaxy bias, the observed power-law form of the galaxy correlation function must emerge from a delicate balance of several competing effects. The low-mass cutoff of $\langle N \rangle_M$, the high-mass slope of $\langle N \rangle_M$, the width of the $P(N|\langle N \rangle)$ distribution, and the spatial distribution of galaxies within halos each affect $\xi(r)$ in different ways. A power-law $\xi(r)$ requires, at the least, a smooth connection between the one-halo and two-halo contributions to the galaxy pair counts and compatible logarithmic slopes in the one-halo and two-halo regimes. Figure 2 shows that the HODs predicted by the SPH and SA models achieve such an alignment, since both methods predict a correlation function that is roughly consistent with a power law for galaxies of space density $\bar{n}_g = 0.02\ h^3\ \mathrm{Mpc}^{-3}$. However, since the emergence of the power law is somewhat fortuitous, we expect that sufficiently precise predictions would show departures from a pure power-law shape. These departures are hidden in Figure 2 by the relatively large error bars, which in turn reflect the limited volume of our single, 50 h^{-1} Mpc simulation cube.

To improve the statistical precision of our $\xi(r)$ predictions, we bootstrap the HOD results derived from this 50 h^{-1} Mpc volume into a larger volume N-body simulation. Since $P(N|M)$ does not depend on the larger scale environment of halos (as shown in § 3.4), the HODs encode all the information needed to create new galaxy distributions that have the clustering properties predicted by the SPH and SA models. We ran an N-body simulation, using version 1.1 of the parallel GADGET code (Springel, Yoshida, & White 2001), with the same cosmological parameters and initial power spectrum used for the SPH and SA models (described in § 2). The simulation follows the evolution of 256^3 dark matter particles in a 112.5 h^{-1} Mpc box, with a particle mass about twice that of dark matter particles in the SPH simulation. The gravitational softening length is
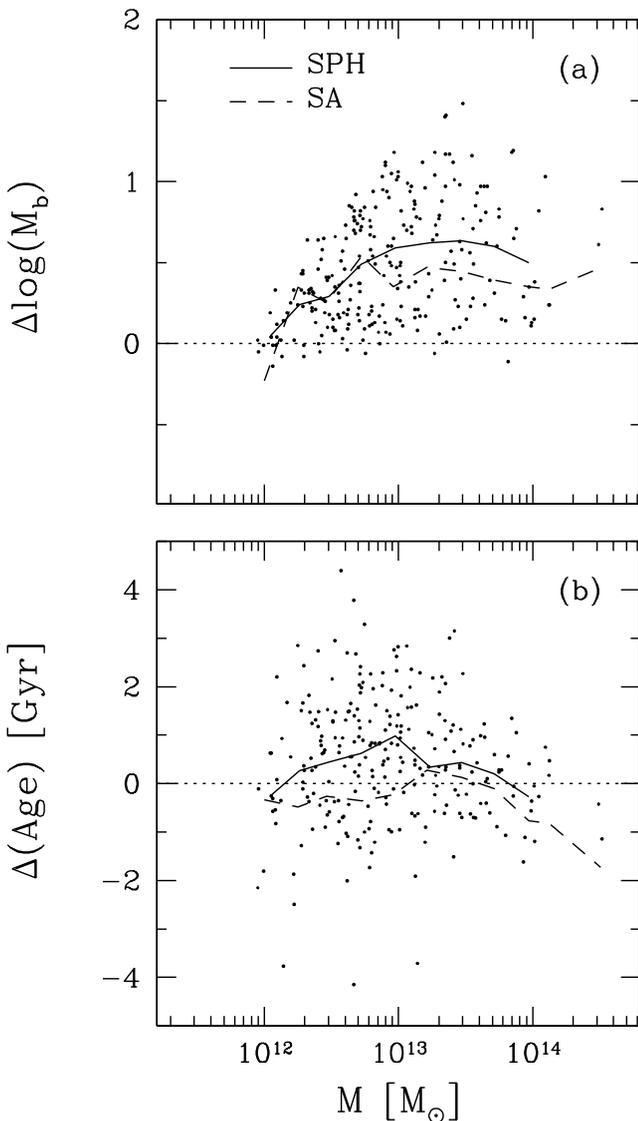

Fig. 20.—(*a*) Difference in log M_b between the central galaxy of each halo and the most massive satellite galaxy. Each point represents an SPH halo. Also shown is the mean logarithmic mass difference for the SPH (*solid curve*) and SA halos (*dashed curve*); (*b*) similar to (*a*), but now showing the difference in age between the central galaxy and the oldest satellite.
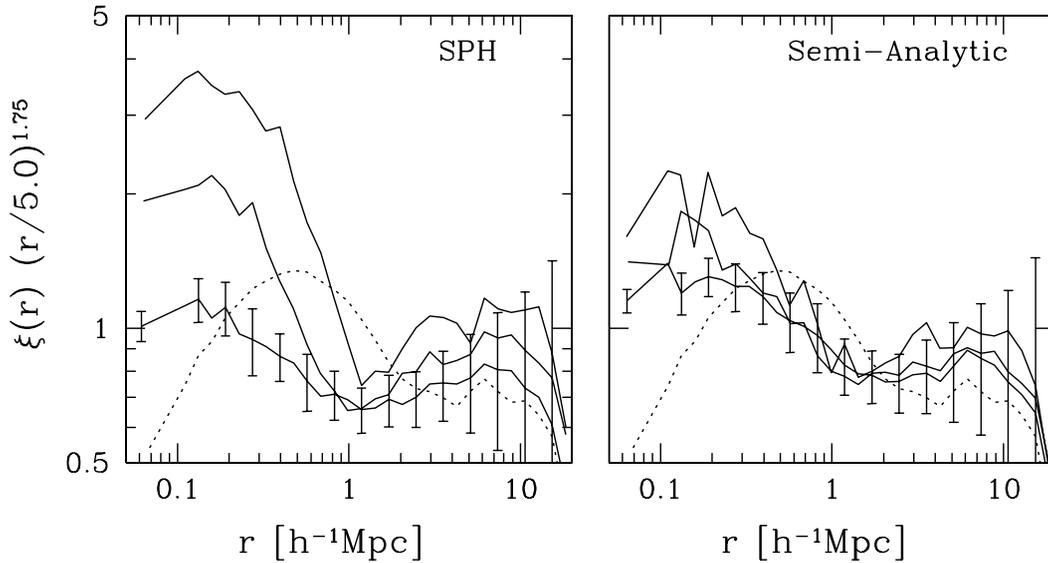
FIG. 21.—Plot of two-point correlation functions, divided by the power law $(r/5.0)^{-1.75}$, computed by applying the predicted SPH (*left*) and SA (*right*) $P(N|M)$ to a larger N-body simulation of the same cosmological model. For each model, the three correlation functions correspond to galaxy populations of space densities $\bar{n}_g = 0.005\ h^3\ \mathrm{Mpc}^{-3}$ (*top curves*), $0.01 h^3\ \mathrm{Mpc}^{-3}$ (*middle curves*), and $0.02\ h^3\ \mathrm{Mpc}^{-3}$ (*bottom curves*). Errors in the mean estimated from jackknife resampling using the eight octants of the cube are shown for the $\bar{n}_g = 0.02\ h^3\ \mathrm{Mpc}^{-3}$ samples. Also shown is the dark matter correlation function of the N-body simulation (*dotted line*).

15 h^{-1} kpc. We identify dark matter halos by using a friends-of-friends algorithm with a linking length of 0.173 times the mean interparticle separation (exactly as we did for the SPH simulation). We populate each halo with a number of galaxies drawn from the $P(N|M)$ distributions predicted by the SPH and SA models. In the high halo mass regime, the SPH model makes no direct prediction of $P(N|M)$ because the simulation volume does not contain enough high-mass halos, and we have not computed SA predictions for halo masses not represented in the simulation. In this regime, therefore, we use the fitting formula of equation (2) with the parameter values in Table 1 to compute $\langle N \rangle$, and we draw a number of galaxies assuming a Poisson $P(N|\langle N \rangle)$ distribution. The latter assumption is reasonable because we have shown that both models predict Poisson pair counts $\langle N(N-1) \rangle_M$ in high-mass halos (Fig. 6). Once we have determined N for a given halo, we place the first galaxy at the center of mass of the halo and any remaining galaxies at the locations of random dark matter particles within the halo. Once again, these are reasonable assumptions given our results on the spatial distribution of galaxies within halos in § 4. In this way, we create galaxy distributions in the 112.5 h^{-1} Mpc box using the HODs predicted by the SPH and SA models for galaxies of space densities $\bar{n}_g = 0.02, 0.01$, and $0.005\ h^3\ \mathrm{Mpc}^{-3}$.

Figure 21 shows the correlation functions for these bootstrapped galaxy distributions. To investigate departures from a power-law shape, we have divided $\xi(r)$ by the power law $(r/5.0)^{-1.75}$, and we use logarithmic axes so that power laws of other slopes would still be straight lines in the plot. Errors in the mean estimated from jackknife resampling using the eight octants of the cube are shown for the $\bar{n}_g = 0.02\ h^3\ \mathrm{Mpc}^{-3}$ samples. The errors are highly correlated, as one can see from the smoothness of the curves relative to the size of the error bars. Nonetheless, these error bars are small enough to reveal interesting features that were not evident before. In all cases, $\xi(r)$ dips below a

power-law extrapolation at $r \sim 1\ h^{-1}$ Mpc, then rises more steeply from $r \sim 1$ to $r \sim 0.2\ h^{-1}$ Mpc before returning to the original power law at still smaller scales. The inflection at $r \sim 1\ h^{-1}$ Mpc arises at the transition between the two-halo term, which flattens (toward smaller r) and eventually cuts off on the scales of halo virial radii, and the one-halo term, which rises steeply for r close to the virial radii of the most massive halos (see, e.g., BW; Fig. 7). The predicted departures are stronger for more massive galaxy samples with lower space densities, and Figure 21 shows that even the small difference between the SPH and SA HODs is enough to have a significant quantitative impact, with the SPH model predicting stronger departures from a power law. For the high space density sample, the difference between the SPH and SA correlation functions is caused mainly by the difference in the high-mass slopes of $\langle N \rangle_M$, but for the low space density samples, differences in the cutoff and plateau regime dominate. We have also investigated the impact on the predicted $\xi(r)$ of assuming a nearest-integer distribution for all halo masses instead of using the true predicted $P(N|\langle N \rangle)$. We find that assuming a Nint distribution at all masses leads to an underestimate of $\xi(r)$ by 10%–20% at $r \lesssim 0.5$ for $\bar{n}_g = 0.02\ h^3\ \mathrm{Mpc}^{-3}$, growing to 30%–40% for the lower space densities.

Figure 22 shows predicted correlation functions for the old and young halves of the SPH and SA $\bar{n}_g = 0.02\ h^3\ \mathrm{Mpc}^{-3}$ samples. As before, these were computed by populating the larger volume N-body simulation with galaxies using the predicted $P(N|M)$ for old and young galaxies (of which the mean occupations are seen in Fig. 13). In the high halo mass regime, where we do not have secure calculations of $P(N|M)$ because of our limited number of halos, we compute $\langle N \rangle$ by extrapolation, and we draw a number of galaxies by assuming a Poisson $P(N|\langle N \rangle)$ distribution. Figure 22 also shows the one-halo terms for old and young galaxies. The most striking difference between old and young galaxies is that the one-halo term for young
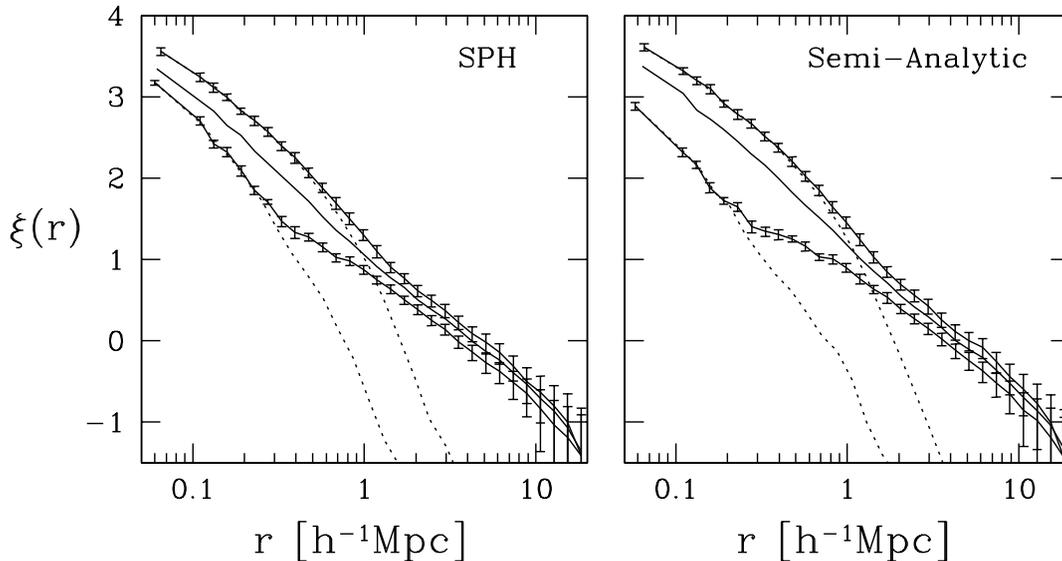
FIG. 22.—Plot of two-point correlation functions of old (*top curves*), young (*bottom curves*), and all (*middle curves*) galaxies in the SPH (*left*) and SA (*right*) models. Correlation functions were computed by applying the predicted $P(N|M)$ for each case to a larger N-body simulation of the same cosmological model. Errors in the mean that were estimated from jackknife resampling using the eight octants of the cube are shown for the young and old halves. Also shown are the one-halo terms (*dotted curves*) for the young and old halves.

galaxies is severely depressed in amplitude compared with that for old galaxies. This depression is caused by a very high fraction of young galaxies that are isolated in their own halos. As a consequence, the one-halo and two-halo terms for young galaxies meet, and thus create a feature in $\xi_g(r)$, at a much smaller scale ($r \sim 0.3\ h^{-1}$ Mpc) than for old galaxies. The depression in the young one-halo term predicted by the SA model is stronger than the SPH one, because of the lower fraction of young galaxies in high-multiplicity halos seen in Figure 13.

Most observational measurements of the galaxy correlation function have appeared consistent with a power law on scales $r \lesssim 5\ h^{-1}$ Mpc (e.g., Norberg et al. 2002a; Zehavi et al. 2002; and numerous references therein), though there have been suggestions of a "shoulder" or flattening in the range $5\ h^{-1}$ Mpc $\lesssim r \lesssim 10\ h^{-1}$ Mpc (e.g., Dekel & Aarseth 1984; Baugh 1996; Gaztañaga & Juszkiewicz 2001; Hawkins et al. 2003). The theoretical predictions (here and in earlier papers) suggest that departures from a pure power law should be measurable at sufficiently high precision, with the generic expectation being an inflection in $\xi(r)$ near the scale of the one-halo to two-halo transition. Motivated in part by these predictions, Zehavi et al. (2003) have recently examined the projected correlation function of luminous ($M_r < -21$) galaxies from the SDSS. They find a statistically significant departure from a power law of just this predicted form. The space density of the Zehavi et al. sample is lower than that of our highest-mass–threshold sample, so we cannot directly test the results shown in Figure 21, but their measurements can be well fitted by an HOD model that is qualitatively similar to that found here. Magliocchetti & Porciani (2003) have shown that the projected correlation functions of 2dFGRS galaxies can also be fitted well by HOD models. As Figures 21 and 22 show, the SPH and SA models make a number of distinctive predictions about the dependence of the correlation function amplitude and shape on galaxy mass and age, and these predictions can be tested in the near future.

7. SUMMARY AND DISCUSSION

The SPH and SA predictions of the galaxy HOD agree remarkably well. The qualitative features of these predictions can, for the most part, be readily interpreted in terms of galaxy formation physics. The mean occupation function for galaxies above a mass threshold has a cutoff, a slowly rising plateau, and a steeper "high occupancy" regime. In the SPH simulation, the cutoff is determined by the universal baryon fraction. In the SA model, the cutoff occurs at a substantially higher mass than the universal baryon fraction requires, corresponding to only $\sim$25% of the gas in low-mass halos remaining in galaxies. This is due to the feedback mechanism, which in the SA model is tuned to produce the observed galaxy luminosity function. The cutoff is nearly as sharp in the SA model as in the SPH simulation because feedback is tightly regulated by halo mass, with no scatter that would allow some low-mass halos to retain substantially more than $\sim$25% of their baryons. In the low-occupancy regime, $\langle N \rangle$ rises slowly with M because additional mass tends to go into making more massive single galaxies instead of multiple low-mass galaxies. The logarithmic slope of $\langle N \rangle_M$ steepens for $\langle N \rangle \gtrsim 2$, presumably representing a transition to a regime in which the galaxies in a halo were formed mostly in the lower mass progenitor halos that merged to create it. Even in this regime, the slope is below unity, since the overall efficiency of galaxy formation (fraction of mass in galaxies) is lower in high-mass halos, probably a consequence of longer cooling times and less efficient filamentary "channeling" of gas into galaxies. For higher baryonic mass thresholds, the mean occupation function shifts horizontally along the $\log M$ axis, so this physical explanation of its form is not sensitive to the particular threshold adopted.

Since the considerations that account for the form of $\langle N \rangle_M$ are quite general, it is perhaps not surprising that the SPH and SA calculations agree. More impressive is the agreement on fluctuations about the mean occupation. Both

calculations predict pair counts well below the expectation for Poisson fluctuations at low mass, close to those of the minimal fluctuation, nearest-integer model. As many authors have emphasized (Benson et al. 2000b; Seljak 2000; Peacock & Smith 2000; Scoccimarro et al. 2001; BW), these sub-Poisson fluctuations are essential in understanding the power-law form of the observed galaxy correlation function. Triple counts are also substantially sub-Poisson, though not minimal, and the two calculations again agree. The explanation of sub-Poisson fluctuations is not trivial, but it clearly has to do with statistics of halo merger histories and the timescales of galaxy mergers following halo mergers. In particular, nearly equal-mass halo mergers are rare enough that one must go substantially above the cutoff mass $M_{\min}$ (by a factor of ~ 10) before one is likely to get two galaxies above the mass threshold in a single halo, instead of one, more massive, galaxy. The probability of empty halos follows the nearest-integer prediction, $P(0|M) = \max(1 - \langle N \rangle_M, 0)$, almost exactly in both models. Because the cutoff of $\langle N \rangle_M$ is somewhat sharper in the SPH calculation, the transition from occupied halos to empty halos (at the specified baryonic mass threshold) is also somewhat sharper, occurring over about a factor of 2 in halo mass. For masses above the cutoff, the probability that a halo is empty is much lower than the Poisson expectation $\exp(-\langle N \rangle_M)$. In this regime, strongly sub-Poisson statistics indicate the regularity of the formation process in single-galaxy halos, which produces a tight correlation between galaxy mass and halo mass.

The mean occupation is very different for galaxies in different age quartiles, at both the low- and high-mass ends of $\langle N \rangle_M$. Young galaxies are rare in high-mass halos and vice versa. This difference reflects a tendency for star formation to begin early in regions that will become part of high-mass halos and for star formation to shut off when a galaxy falls into a halo of larger virial mass, or to slow down when the halo size or virial temperature becomes too large. The qualitative agreement between the SPH and SA calculations is again not surprising, but the degree of quantitative agreement is impressive.

The SPH simulation also shows that the mean occupation function is independent of the large-scale environment of the halo, extending to the galaxy regime the result that Lemson & Kauffmann (1999) found for the merger histories of dark matter halos. This is a fundamental and encouraging result, supporting the assumption made in merger tree–based SA methods, and supporting the claim that the HOD provides a statistically complete description of galaxy bias.

A detailed analysis of the SPH simulation also supports simple assumptions about the galaxy distribution within halos. Most halos have a galaxy near the center of mass moving at close to the center-of-mass velocity. The central galaxy is almost always the most massive galaxy in the halo, and it is usually among the oldest galaxies in the halo. The remaining, satellite galaxies have the same spatial and velocity distribution as the dark matter, except for a small ($\alpha_v \sim 0.8$–0.95) velocity bias in intermediate-mass halos. These assumptions are thus reasonable to use when making galaxy-clustering predictions, and they are the ones usually incorporated in studies that combine N-body and semianalytic methods (Kauffmann et al. 1999; Benson et al. 2000b; Somerville et al. 2001). In the long term, these predictions can be tested empirically using clustering and galaxy-galaxy lensing data of the sort provided by 2dFGRS and SDSS.

As we have emphasized in separate papers on the SA model and SPH simulation (Benson et al. 2000b; Weinberg et al. 2002), the complex relation between galaxies and mass is crucial in reproducing the observed nearly power-law form of the galaxy correlation function, since the dark matter $\xi(r)$ is not a power law in CDM-type models. Since the emergence of the power law is to some extent a coincidence, the HOD framework generically predicts that there should be departures from a power law, $\xi(r)$, once it is measured with sufficient precision, especially if one considers different subclasses of galaxies. We have tried to predict these departures by bootstrapping our results into a larger volume N-body simulation. The small differences between the SA and SPH $P(N|M)$ translate into noticeable differences in the predicted $\xi(r)$, and the accuracy of the SPH prediction is still limited to some extent by the small number of high-mass halos in the SPH volume. However, improved statistics show that both models predict an inflection in $\xi(r)$ at $r \sim 1$ h^{-1} Mpc, with the departures from a power law being stronger for the SPH model than for the SA model and stronger for more massive galaxies in both cases. Recent observational analyses provide evidence for just such a feature in the correlation function of luminous galaxies (Zehavi et al. 2003).

The most surprising aspect of our results is that the SPH and SA models give such similar predictions for $P(N|M)$ despite having very different galaxy mass functions. The different mass functions reflect the different treatments of cooling in the SA and SPH calculations (including the geometric idealizations in the former and the numerical resolution limitations in the latter) and the greater importance of stellar feedback in the SA calculation. The similarity of the predicted halo occupations implies that the HOD is determined by physics that is robust to these cooling and feedback differences. Obviously it is crucial that we select galaxy samples on the basis of number density, using only the rank order of the baryonic masses rather than their absolute values; for a fixed mass threshold, the numbers of galaxies would be different in the two calculations, and the HODs could not possibly match. Similarity of HODs suggests that the rank order of galaxy masses and the rank order of stellar population ages are related in fairly simple ways to the merger histories of the dark matter halos, which should be statistically similar in the two methods. For example, the baryonic mass of a galaxy could be monotonically related (by nonlinear functions that are different in the two calculations) to the mass of its parent halo at the last time this galaxy was "central." The age could be determined (at least in a rank-order sense) by the formation time of this halo and the time at which its central object's star formation is suppressed by falling into a larger halo and becoming a satellite. Mergers within halos also affect $P(N|M)$, but this process should be similar in the two calculations, since the assumptions about mergers in the SA model reproduce the results of numerical calculations (Benson et al. 2002).

We can test the idea that the form of the HOD is driven largely by dark matter dynamics by reanalyzing the SA galaxy population without using the predicted baryonic properties. For every SA galaxy, we identify its parent halo at the last time this galaxy was central, and we denote the halo mass at that time by $M_{\max}$ and the time itself by $t_{\max}$. We then create galaxy samples with the same space densities as before but use thresholds in $M_{\max}$ rather than in baryonic mass. Dotted curves in Figures 9 and 10 show the first and
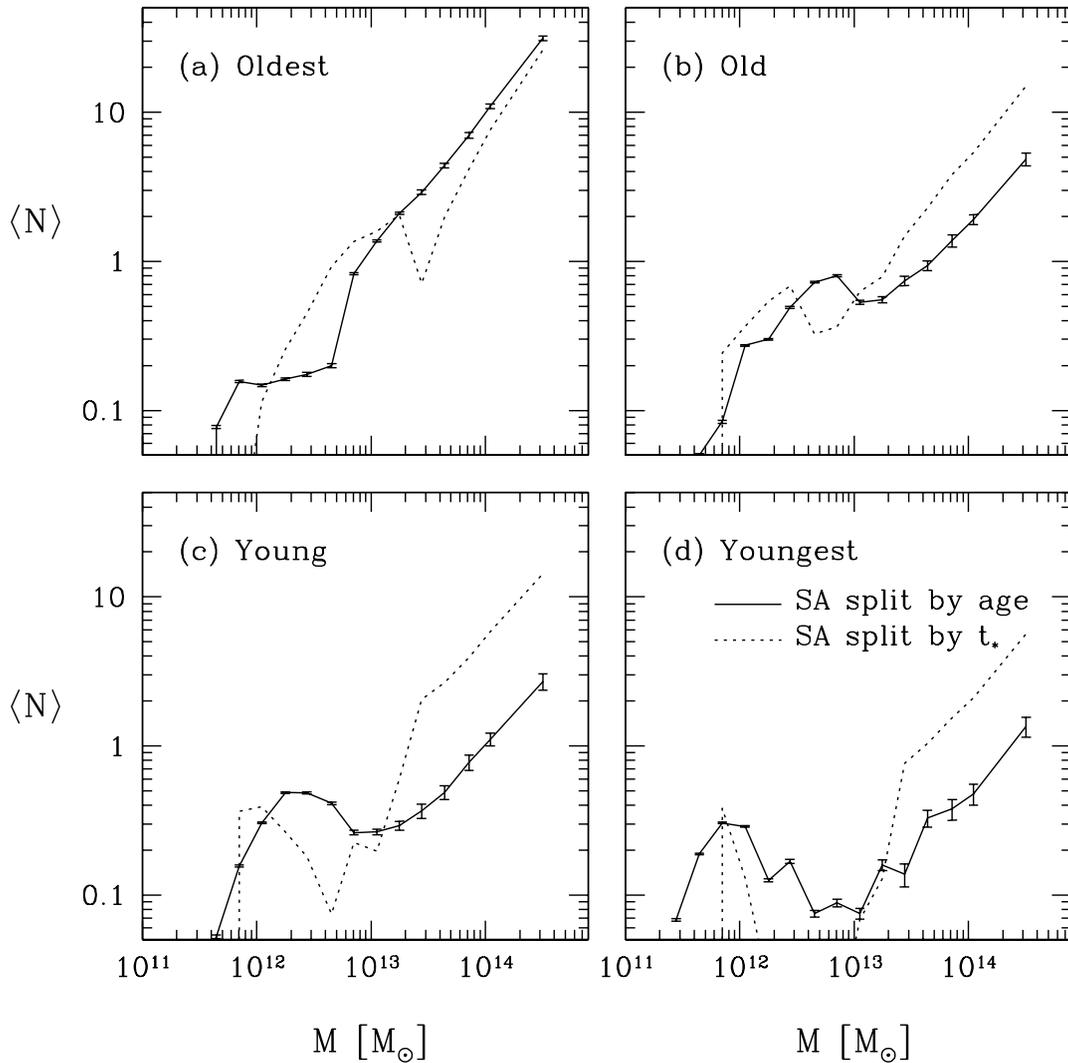
Fig. 23.—Mean occupation $\langle N \rangle_M$ of SA galaxies, for quartiles of mean stellar galaxy age (*solid curves*) and merger tree "age" parameter t_* (*dashed curves*; defined in § 7).

second moments of $N(M)$, respectively, for these samples defined by M_{max} thresholds. It is interesting both that this simple mapping works as well as it does and that it does not work perfectly. The qualitative similarity of the mean occupations supports the idea that $P(N|M)$ is largely governed by robust physics connected to halo merger histories. However, obvious differences, in particular the steeper slope of $\langle N \rangle_M$ at the high-mass end, indicate that additional physical processes must also play a significant role. It is encouraging that the SPH and SA models agree with each other better than either model agrees with the "rank by M_{max}" calculation. The fact that they predict fewer galaxies in high-mass halos suggests that galaxy accretion rates begin to drop in overdense environments even before their parent halos fall into larger halos, allowing some of these galaxies to drop below the baryonic mass threshold and be replaced (in a sample of fixed space density) by galaxies forming in lower mass halos. Recent studies provide observational support for this effect, showing decreased star formation rates in galaxies that are well outside the virial radii of rich clusters (e.g., Lewis et al. 2002; Gomez et al. 2003).

We can map the stellar age of a galaxy onto the halo merger tree in a similar fashion. We make the simple assumption that the star formation in each galaxy starts at a time t_{start} when its parent halo first exceeds a mass $10^{11} \, M_\odot$, a factor of ~ 4 below the cutoff for $\bar{n}_g = 0.02 \, h^3 \, \mathrm{Mpc}^{-3}$. We assume that the star formation ends at a time t_{stop} when the galaxy becomes a satellite ($t_{stop} = t_{max}$) or when the cooling time in its parent halo becomes too long ($t_{stop} = t_{hot}$), whichever happens first. We identify t_{hot} as the time when the parent halo mass exceeds $10^{13} \, M_\odot$. Finally, we assume a constant star formation rate between t_{start} and t_{stop}, making the mean stellar age of the galaxy $t_* = t_0 - (t_{stop} - t_{start})/2$. Figure 23 compares the mean occupation functions for SA galaxies split into quartiles according to t_* with those of quartiles defined by true stellar age (repeated from Fig. 11). Our highly simplified approximation yields the right qualitative dependence of $\langle N \rangle_M$ on galaxy age, but it differs substantially in the quantitative details. The M_{max} and t_* models still make indirect use of the baryonic physics in the SA calculation, since baryonic masses affect which galaxies remain as distinct entities in larger halos and which are

destroyed by dynamical friction. Results from a more concerted effort to model the HOD entirely with dark matter dynamics will be reported elsewhere (A. V. Krautsov et al. 2003, in preparation).

Finite resolution of the SPH simulation has limited our comparison of predictions with relatively massive galaxies, and with age rather than morphology as a distinguishing characteristic of subclasses. Insensitivity of predictions to details of calculation is likely to change when one gets to low-mass galaxies or to characteristics that are determined by interactions with environment. For example, we might expect the HOD of low-mass galaxies to be quite different if their luminosity is controlled by photoionization or by supernova feedback. Likewise, models that ascribe bulge-to-disk ratios mainly to merger histories, to secular evolution of disks, to weak perturbations in group/cluster environments, or to interaction with the intergalactic medium could yield quite different predictions for the $P(N|M)$ of different morphological types. The process of inferring halo occupations from observed galaxy clustering has already begun, and it should accelerate over the next few years with improved measurements from the 2dFGRS and the SDSS. Empirical HOD determinations for galaxies with $L \gtrsim L_*$, classified by luminosity and color or spectral type, will test the basic predictions of the current scenario of galaxy formation, as presented here. They will also sharpen the constraints on cosmological models by removing bias as a degree of freedom in matching observed clustering. Empirical determinations of HODs for faint galaxies and for morphological subtypes should yield insight into the physics that governs the low end of the luminosity function and the origin of galaxy morphology.

REFERENCES

Avila-Reese, V., Firmani, C., & Hernandez, X. 1998, ApJ, 505, 37
Baugh, C. M. 1996, MNRAS, 280, 267
Benson, A. J. 2001, MNRAS, 325, 1039
Benson, A. J., Baugh, C. M., Cole, S., Frenk, C. S., & Lacey, C. G. 2000a, MNRAS, 316, 107
Benson, A. J., Cole, S., Frenk, C. S., Baugh, C. M., & Lacey, C. G. 2000b, MNRAS, 311, 793
Benson, A. J., Lacey, C. G., Baugh, C. M., Cole, S., & Frenk, C. S. 2002, MNRAS, 333, 156
Berlind, A. A., & Weinberg, D. H. 2002, ApJ, 575, 587 (BW)
Blanton, M. R., et al. 2001, AJ, 121, 2358
Bond, J. R., Cole, S., Efstathiou, G., & Kaiser, N. 1991, ApJ, 379, 440
Bullock, J. S., Wechsler, R. H., & Somerville, R. S. 2002, MNRAS, 329, 246
Cen, R., & Ostriker, J. P. 1992, ApJ, 399, L113
———. 2000, ApJ, 538, 83
Cole, S. 1991, ApJ, 367, 45
Cole, S., Aragon-Salamanca, A., Frenk, C. S., Navarro, J. F., & Zepf, S. E. 1994, MNRAS, 271, 781
Cole, S., Lacey, C. G., Baugh, C. M., & Frenk, C. S. 2000, MNRAS, 319, 168
Colless, M., et al. 2001, MNRAS, 328, 1039
Colombi, S., Szapudi, I., Jenkins, A., & Colberg, J. 2000, MNRAS, 313, 711
Cooray, A. 2002, ApJ, 576, L105
Cooray, A., & Sheth, R. 2002, Phys. Rep., 372, 1
Croft, R. A. C., Di Matteo, T., Davé, R., Hernquist, L., Katz, N., Fardal, M., & Weinberg, D. H. 2001, ApJ, 557, 67
Davé, R., Dubinski, J., & Hernquist, L. 1997, NewA, 2, 277
Davé, R., Katz, N., & Weinberg, D. H. 2002, ApJ, 579, 23
Davis, M., Efstathiou, G., Frenk, C. S., & White, S. D. M. 1985, ApJ, 292, 371
Dekel, A., & Aarseth, S. J. 1984, ApJ, 283, 1
Diaferio, A., Kauffmann, G., Colberg, J. M., & White, S. D. M. 1999, MNRAS, 307, 537
Evrard, A. E., Summers, F. J., & Davis, M. 1994, ApJ, 422, 11
Fall, S. M., & Efstathiou, G. 1980, MNRAS, 193, 189
Gaztañaga, E., & Juszkiewicz, R. 2001, ApJ, 558, L1
Gomez, P., et al. 2003, ApJ, 584, 210
Governato, F., Baugh, C. M., Frenk, C. S., Cole, S., Lacey, C. G., Quinn, T., & Stadel, J. 1998, Nature, 392, 359
Guzik, J., & Seljak, U. 2002, MNRAS, 335, 311
Hawkins, E., et al. 2003, MNRAS, submitted (astro-ph/0212375)
Helly, J. C., Cole, S., Frenk, C. S., Baugh, C. M., Benson, A., Lacey, C., & Pearce, F. R. 2003, MNRAS, 338, 913
Hernquist, L., & Katz, N. 1989, ApJS, 70, 419
Jenkins, A., et al. 1998, ApJ, 499, 20
Jing, Y. P., Börner, G., & Suto, Y. 2002, ApJ, 564, 15
Jing, Y. P., Mo, H. J., & Börner, G. 1998, ApJ, 494, 1
Katz, N., Hernquist, L., & Weinberg, D. H. 1992, ApJ, 399, L109
Katz, N., Keres, D., Davé, R., & Weinberg, D. H. 2003a, in The IGM/Galaxy Connection, ed. M. Putman & J. Rosenberg (Dordrecht: Kluwer), 185
Katz, N., Quinn, T., Bertschinger, E., & Gelb, J. M. 1994, MNRAS, 270, L71
Katz, N., Weinberg, D. H., & Hernquist, L. 1996, ApJS, 105, 19
Kauffmann, G., Colberg, J. M., Diaferio, A., & White, S. D. M. 1999, MNRAS, 303, 188
Kauffmann, G., Nusser, A., & Steinmetz, M. 1997, MNRAS, 286, 795
Kauffmann, G., White, S. D. M., & Guideroni, B. 1993, MNRAS, 264, 201
Kochanek, C. S., White, M., Huchra, J., Macri, L., Jarrett, T. H., Schneider, S. E., & Mader, J. 2003, ApJ, 585, 161
Lacey, C. G., & Cole, S. 1993, MNRAS, 262, 627
Lacey, C., & Silk, J. 1991, ApJ, 381, 14
Lemson, G., & Kauffmann, G. 1999, MNRAS, 302, 111
Lewis, I., et al. 2002, MNRAS, 334, 673
Ma, C., & Fry, J. N. 2000, ApJ, 543, 503
Magliocchetti, M., & Porciani, C. 2003, MNRAS, submitted (astro-ph/0304003)
Marinoni, C., & Hudson, M. J. 2002, ApJ, 569, 101
McClelland, J., & Silk, J. 1977, ApJ, 217, 331
McKay, T. A., et al. 2001, preprint (astro-ph/0108013)
Miller, G. E., & Scalo, J. M. 1979, ApJS, 41, 513
Mo, H. J., & White, S. D. M. 1996, MNRAS, 282, 1096
Moustakas, L. A., & Somerville, R. S. 2002, ApJ, 577, 1
Murali, C., Katz, N., Hernquist, L., Weinberg, D. H., & Davé, R. 2002, ApJ, 571, 1
Navarro, J. F., Frenk, C. S., & White, S. D. M. 1996, ApJ, 462, 563
Neyman, J., & Scott, E. L. 1952, ApJ, 116, 144
Norberg, P., et al. 2002a, MNRAS, 332, 827
———. 2002b, MNRAS, 336, 907
Peacock, J. A., & Smith, R. E. 2000, MNRAS, 318, 1144
Pearce, F. R., Jenkins, A., Frenk, C. S., White, S. D. M., Thomas, P. A., Couchman, H. M. P., Peacock, J. A., & Efstathiou, G. 2001, MNRAS, 326, 649
Pearce, F. R., et al. 1999, ApJ, 521, L99
Peebles, P. J. E. 1974, A&A, 32, 197
Press, W. H., & Schechter, P. 1974, ApJ, 187, 425
Scherrer, R. J., & Bertschinger, E. 1991, ApJ, 381, 349
Scoccimarro, R., Sheth, R. K., Hui, L., & Jain, B. 2001, ApJ, 546, 20
Scranton, R. 2002, MNRAS, 332, 697
Seljak, U. 2000, MNRAS, 318, 203
Sheth, R. K., & Diaferio, A. 2001, MNRAS, 322, 901
Sheth, R. K., Diaferio, A., Hui, L., & Scoccimarro, R. 2001a, MNRAS, 326, 463
Sheth, R. K., Mo, H. J., & Tormen, G. 2001b, MNRAS, 323, 1
Somerville, R. S., Lemson, G., Sigad, Y., Dekel, A., Kauffmann, G., & White, S. D. M. 2001, MNRAS, 320, 289
Somerville, R. S., & Primack, J. R. 1999, MNRAS, 310, 1087
Spergel, D. N., et al. 2003, ApJ, submitted (astro-ph/0302209)
Springel, V., & Hernquist, L. 2002, MNRAS, 333, 649
Springel, V., Yoshida, N., & White, S. D. M. 2001, NewA, 6, 79
Tully, R. B., & Fisher, J. R. 1977, A&A, 54, 661
van den Bosch, F. C., Yang, X., & Mo, H. J. 2003, MNRAS, 340, 771
Wechsler, R. H., Somerville, R. S., Bullock, J. S., Kolatt, T. S., Primack, J. R., Blumenthal, G. R., & Dekel, A. 2001, ApJ, 554, 85
Weinberg, D. H. 2002, in ASP Conf. Ser. 283, A New Era in Cosmology, ed. T. Shanks & N. Metcalfe (San Francisco: ASP)
Weinberg, D. H., Davé, R., Katz, N., & Hernquist, L. 2002, ApJ, submitted
Weinberg, D. H., Hernquist, L., & Katz, N. 1997, ApJ, 477, 8
White, M. 2001, MNRAS, 321, 1
White, M., Hernquist, L., & Springel, V. 2001, ApJ, 550, L129
White, S. D. M. 1996, in Cosmology and Large Scale Structure, ed. R. Schaefer, J. Silk, M. Spiro, & J. Zinn-Justin (Dordrecht: Elsevier)
White, S. D. M., & Frenk, C. S. 1991, ApJ, 379, 52

White, S. D. M., & Rees, M. J. 1978, MNRAS, 183, 341
Yang, X., Mo, H. J., & van den Bosch, F. C. 2003, MNRAS, 339, 1057
York, D. G., et al. 2000, AJ, 120, 1579
Yoshida, N., Stoehr, F., Springel, V., & White, S. D. M. 2002, MNRAS, 335, 762
Yoshikawa, K., Taruya, A., Jing, Y. P., & Suto, Y. 2001, ApJ, 558, 520

Zehavi, I., et al. 2002, ApJ, 571, 172
———. 2003, ApJ, submitted (astro-ph/0301280)
Zheng, Z., Tinker, J. L., Weinberg, D. H., & Berlind, A. A. 2002, ApJ, 575, 617